UNIVERSITY OF ALBERTA

Effects of Bonding Layer Properties on the Dynamic Behaviour of Piezoelectric Sensors/Actuators

by

Lu Han

A thesis submitted to the Faculty of Graduate Studies and Research in partial fulfillment of the requirements for the degree of Master of Science

Department of Mechanical Engineering

Edmonton, Alberta

Spring 2008

Library and Archives Canada

Published Heritage Branch

395 Wellington Street
Ottawa ON K1A 0N4
Canada

Bibliothèque et Archives Canada

Direction du Patrimoine de l'édition

395, rue Wellington
Ottawa ON K1A 0N4
Canada

Your file Votre référence
ISBN: 978-0-494-45814-3
Our file Notre référence
ISBN: 978-0-494-45814-3

NOTICE:
The author has granted a non-exclusive license allowing Library and Archives Canada to reproduce, publish, archive, preserve, conserve, communicate to the public by telecommunication or on the Internet, loan, distribute and sell theses worldwide, for commercial or non-commercial purposes, in microform, paper, electronic and/or any other formats.

The author retains copyright ownership and moral rights in this thesis. Neither the thesis nor substantial extracts from it may be printed or otherwise reproduced without the author's permission.

AVIS:
L'auteur a accordé une licence non exclusive permettant à la Bibliothèque et Archives Canada de reproduire, publier, archiver, sauvegarder, conserver, transmettre au public par télécommunication ou par l'Internet, prêter, distribuer et vendre des thèses partout dans le monde, à des fins commerciales ou autres, sur support microforme, papier, électronique et/ou autres formats.

L'auteur conserve la propriété du droit d'auteur et des droits moraux qui protège cette thèse. Ni la thèse ni des extraits substantiels de celle-ci ne doivent être imprimés ou autrement reproduits sans son autorisation.

In compliance with the Canadian Privacy Act some supporting forms may have been removed from this thesis.

While these forms may be included in the document page count, their removal does not represent any loss of content from the thesis.

Conformément à la loi canadienne sur la protection de la vie privée, quelques formulaires secondaires ont été enlevés de cette thèse.

Bien que ces formulaires aient inclus dans la pagination, il n'y aura aucun contenu manquant.

Canada

Abstract

The performance of smart structures depends on the dynamic electromechanical behaviour of piezoelectric sensors/actuators and the bonding condition along the interface, which connects the sensor/actuator and the host structures. This thesis documents a theoretical study of the influence of material parameters of the bonding layer on the coupled electromechanical characteristics of piezoelectric sensors/actuators, which are subjected to high frequency mechanical loads or electric loads. A one dimensional sensor/actuator model with a bonding layer, which undergoes a shear deformation, is proposed. Analytical solutions based on the integral equation method are provided. Detailed numerical simulation is conducted to evaluate the effect of the bonding layer under different loading frequencies. The results indicate that, the properties of the bonding layer, the loading frequency, the material combination and the geometry of the sensor/actuator have significant effects on the load transfer between the sensor/actuator and the host medium.

ACKNOWLEDGEMENTS

I would like express my deepest gratitude to Dr. Xiaodong Wang, my supervisor, for his constant encouragement and guidance. His trust, support and invaluable advice made every stage of my research work go smoothly and pleasantly. My grateful sentiments come from the bottom of my heart.

Secondly, I would like to express my sincere appreciation to my co-supervisor, Dr. Ming J. Zuo, for his constant guidance and precious suggestions about my studies and research work.

Thirdly, my thanks would go to my parents and my sister. Their support, understanding and endless love are the source of my courage and strength to conquer any difficulty in my study and life.

Finally but not least, I would like to thank all my friends, who share their time with me, listen to me, and help me out during tough periods.

CONTENTS

1 Introduction **1**

1.1 Background 1

1.2 Research Objectives 4

1.3 Organization of the Thesis 4

2 Literature Review **5**

2.1 Piezoelectricity and Piezoelectric Ceramics 5

2.2 Global Response of the Piezoelectric Systems 6

2.3 Electromechanical Impedance Techniques 8

2.4 Elastic Wave Propagation in Piezoelectric Systems . . 9

2.5 The Local Stress Field Around Piezoelectric Patches . 10

2.6 Studies on the Bonding Layers in Low Frequency Cases 12

2.7 Summary 13

3 Analysis of the Piezoelectric Sensor system **14**

3.1 Formulation of the Problem 14

3.1.1 Modelling of the Bonding Layer 17

3.1.2 The Dynamic Sensor Model 18

3.1.3 Dynamic Behaviour of the Host Medium 23

3.1.4 Dynamic Load Transfer 28

3.2 Results and Discussion 31
3.2.1 Wave Propagation Inside the Host Medium 32
3.2.2 Strain Distribution Along the Sensor 33
3.2.3 Output Voltage of the Sensor 44
3.3 Concluding Remarks 53

4 Analysis of the Piezoelectric Actuator System 57
4.1 Formulation of the Problem 58
4.1.1 The Bonding Layer 60
4.1.2 Modelling of the Actuator 60
4.1.3 Dynamic Behaviour of the Host Medium 62
4.1.4 Dynamic Load Transfer 63
4.2 Results and Discussion 66
4.2.1 The Effect of the Thickness of the Bonding Layer 67
4.2.2 The Effect of the Coefficient of Viscosity 69
4.2.3 The Effect of the Loading Frequency 70
4.2.4 The Effect of the Material Mismatch 71
4.2.5 The Effect of the Geometry of the Actuator 73
4.3 Concluding Remarks 75

5 Conclusions and Future Work 78
5.1 Contributions and Conclusions 78
5.2 Future Work 81

Bibliography 83

Appendix 94

List of Tables

3.1 Material Properties of the PZT Sensor/Actuator 32

3.2 Material Properties of the Host Medium and the Bonding Layer-Sensor System 32

4.1 Material Properties of the Host Medium and the Bonding Layer-Actuator System 67

List of Figures

1.1 Experimental set-up of aluminum beam samples for damage detection. (a) Aluminum beam samples; (b) Detail of damages, sensor and actuator locations [4] 3

3.1 Geometry of the sensor system 16

3.2 Stress fields of the sensor system 16

3.3 Stress field inside of the sensor 20

3.4 The stress field inside of the host medium-sensor system 24

3.5 Normalized strain distribution along the sensor (ka=1.0, q=0.3928, v=20.0, $c_b = 10$) 36

3.6 Normalized strain distribution along the sensor (ka=4.0, q=0.3928, v=20.0, $c_b = 10$) 37

3.7 Normalized strain distribution along the sensor (ka=8.0, q=0.3928, v=20.0, $c_b = 10$) 38

3.8 The phase angle of the dynamic strain ratio θ^0 (ka=1.0, q=0.3928, v=20.0, $c_b = 10$) 39

3.9 The phase angle of the dynamic strain ratio θ^0 (ka=4.0, q=0.3928, v=20.0, $c_b = 10$) 40

3.10 The phase angle of the dynamic strain ratio θ^0 (ka=8.0, q=0.3928, v=20.0, $c_b = 10$) 41

3.11 Normalized strain distribution with different coefficients of viscosity ($ka = 1.0$, $h' = 100$, $q = 0.3928$, $v = 20.0$) 42
3.12 Normalized strain distribution with different loading frequencies ($h' = 0$, $q = 0.3928$, $v = 20.0$) 43
3.13 Normalized strain distribution with different loading frequencies ($h' = 100$, $q = 0.3928$, $v = 20.0$, $c_b = 10$) 44
3.14 Normalized strain distribution along the sensor with different material combinations (ka=1.0, h'=0, v=20.0) 45
3.15 Normalized strain distribution along the sensor with different material combinations (ka=1.0, h'=100, v=20.0, c_b=10) 46
3.16 Normalized strain distribution along the sensor with different sensor geometries (ka=1.0, h'=0, q=0.3928) 47
3.17 Normalized strain distribution along the sensor with different sensor geometries (ka=1.0, h'=100, q=0.3928, c_b=10) 48
3.18 Normalized output voltage with different thicknesses of the bonding layer and loading frequencies ($q = 0.3928$, $v = 20.0$, $c_b = 10$) 50
3.19 Normalized output voltage with different loading frequencies and material combinations ($h' = 0$, $v = 20.0$) 52
3.20 Normalized output voltage with different loading frequencies and material combinations ($h' = 100$, $v = 20.0$, $c_b = 10$) 53
3.21 Normalized output voltage with different loading frequencies and sensor geometries ($h' = 0$, $q = 0.3928$) 54
3.22 Normalized output voltage with different loading frequencies and sensor geometries ($h' = 100$, $q = 0.3928$, $c_b = 10$) 55

4.1 Geometry of the actuator system 59
4.2 Stress fields of the actuator system 59

4.3 Normalized shear stress distribution along the actuator with different thicknesses of the bonding layer (ka = 1.0, q = 1.0, v = 20.0, c_b = 10) 68

4.4 Normalized shear stress distribution along the actuator with different thicknesses of the bonding layer (ka=4.0, q = 1.0, v = 20.0, c_b = 10) 69

4.5 Normalized shear stress distribution along the actuator with different thicknesses of the bonding layer (ka=8.0, q = 1.0, v = 20.0, c_b = 10) 70

4.6 Normalized shear stress distribution with different coefficients of viscosity (ka = 5.0, h' = 100, q = 1.0, v = 20.0) 71

4.7 Normalized shear stress distribution with different loading frequencies (h' = 0, q = 1.0, v = 20.0) 72

4.8 Normalized shear stress distribution with different loading frequencies (h' = 100, q = 1.0, v = 20.0, c_b = 10) 73

4.9 Normalized shear stress distribution along the actuator with different material combinations (ka = 5.0, h' = 0, v = 20.0) . . . 74

4.10 Normalized shear stress distribution along the actuator with different material combinations (ka = 5.0, h' = 100, v = 20.0, c_b = 10) 75

4.11 Normalized shear stress distribution with different actuator geometries (ka = 5.0, h' = 0, q = 1.0) 76

4.12 Normalized shear stress distribution with different actuator geometries (ka = 5.0, h' = 100, q = 1.0, c_b = 10) 77

A.1 Reflection of a P-wave 95

List of Symbols

α	Half length of the sensor/actuaor
h	Thickness of the sensor/actuator
h'	Thickness of the bonding layer
ω	Loading frequency
θ_0	Angle of the incident wave to the vertical line
k_L, k_T	Longitudinal wave number, transverse wave number
c_L, c_T	Longitudinal wave speed, transverse wave speed
$\overline{u}_{ij}$	Displacement
u_{ij}	Magnitude of displacement
$\overline{\sigma}_{ij}$	Stress
σ_{ij}	Magnitude of stress
$\overline{\tau}$	Shear stress
τ	Magnitude of shear stress
$\overline{\varepsilon}_{ij}$	Strain
ε_{ij}	Magnitude of strain
D_z	Magnitude of electric displacement
E_z	Magnitude of electric field intensity
c_{ij}	Elastic constant of piezoelectric material
e_{ij}	Piezoelectric constant of piezoelectric material
λ_i	Dielectric constant of piezoelectric material
E_h	Young's Modulus of the host medium
ν_h	Poisson's ratio of the host medium
μ_b	Shear modulus of the bonding layer
c_b	Coefficient of viscosity of the bonding layer
ρ_s, ρ_a, ρ_h	Mass density of the sensor, the actuator, and the host medium
q	Material mismatch factor
v	Sensor/actuator geometry parameter

Chapter 1

Introduction

1.1 Background

Critical engineering structures deteriorate with time as a result of the aging of material, inadequate maintenance, excessive use, etc. In order to prolong the lifespan of a structure and prevent catastrophic failure, these structures need to be monitored constantly for their integrity and health condition. A reliable and efficient structural health monitoring (SHM) system is needed for this purpose. Especially for structures like space shuttles and underground infrastructures, SHM systems that can operate on in-service structures under an isolated environment with minimum human involvement are required. Motivated by this, significant efforts have been made to the development of sensors and actuators, which can be surface-bonded or embedded into the structures, thus used in the in-situ monitoring of structures.

Piezoelectric materials are low in cost, and can be easily fabricated into different desired shapes, or wired into sensor or actuator arrays. As a result, their use as sensors or actuators in SHM systems have been clearly increased in the past few decades [1, 2, 3]. Besides, their quick response to electrical or mechanical changes and high sensitivity to a wide range of loading frequen-

cies make them suitable for dynamic applications. A typical example of the experimental set-up of using piezoelectric patches as sensors or actuators for structure damage detection is shown in Figure 1.1 [4].

One of the most commonly adopted strategies in building SHM systems is to surface-bond piezoelectric patches to the host structures. The material discontinuity between the sensors/actuators and the host structure results in a complicated stress field, especially around the edges of the sensors/actuators, where stress concentration will occur. Therefore, a better understanding of the coupled electromechanical hebaviour of the piezoelectric structures requires a detailed study of the local stress field.

Many works have been done to study the localized stress field generated around the sensors/actuators [5]-[8]. However, in most of the studies, the sensors/actuators are assumed to be perfectly bonded to the host structures, and the effects of the bonding layer on the load transfer between the host structure and the piezoelectric patches have been neglected. The typical material used for bonding piezoelectric sensors/actuators to the host structure is epoxy, or conductive epoxy, whose modulus is much lower than that of the sensors/actuators and the host medium. Therefore, the bonding layer may have significant effects on the property of the integrated system when the thickness of the layer increases, especially for damage detection problems. In most damage detection cases, high frequency elastic waves, which have wave lengthes comparable with or shorter than the length of the sensors/actuators, are generated. Under these circumstances, the existence of the bonding layer may result in even more complicated local stress fields around the sensors/actuators. A more comprehensive understanding of how the bonding layer affects the property of the system is required in order to minimize its effects and optimize the

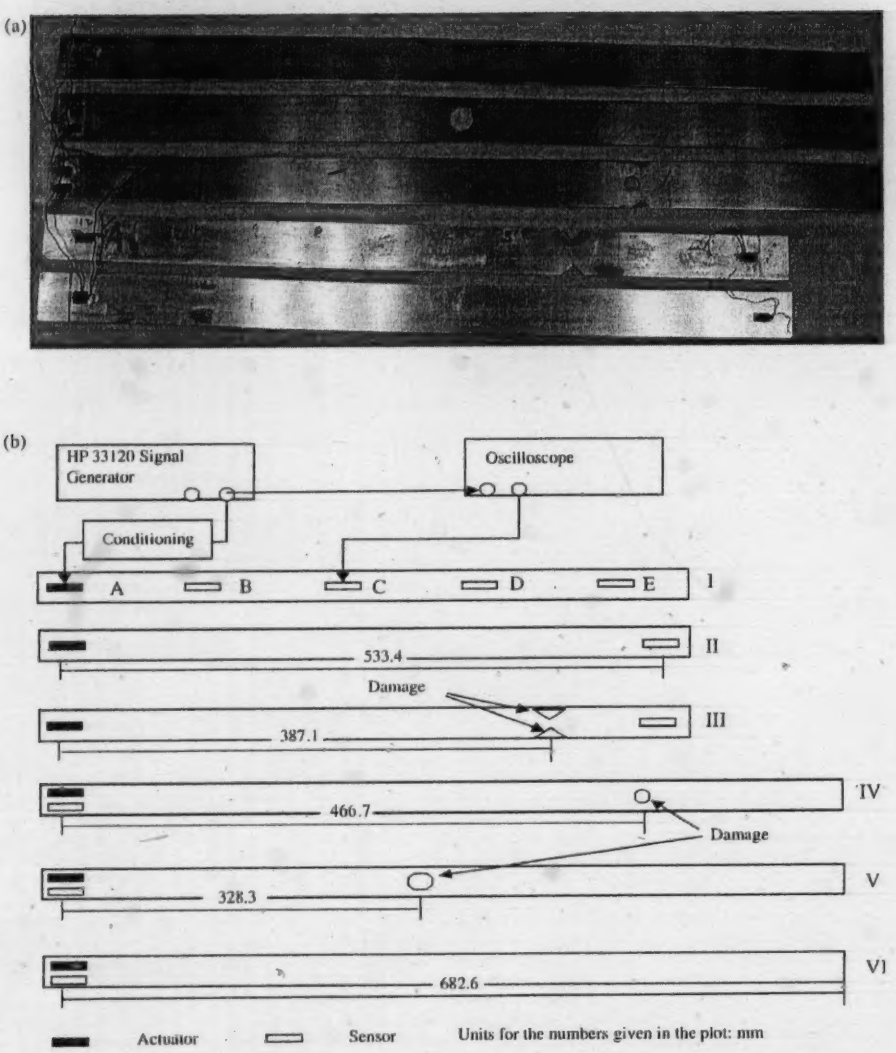

Figure 1.1: Experimental set-up of aluminum beam samples for damage detection. (a) Aluminum beam samples; (b) Detail of damages, sensor and actuator locations [4]

adhesive selection.

1.2 Research Objectives

The objective of this thesis is to study of effects of the bonding layer on the load transfer between a surface-bonded piezoelectric sensor/actuator and the elastic host medium, when the system is subjected to high frequency mechanical or electric loads. To model the electromechanical behaviour of the integrated system, a one dimensional sensor/actuator model will be established. Numerical simulation will be conducted to evaluate the effects of different material properties of both the bonding layer and the sensor/actuator, loading frequencies, and the sensor/actuator geometries on the dynamic electromechanical characteristics of the sensor/actuator under high frequency dynamic loads.

1.3 Organization of the Thesis

The thesis is organized as follow. The current progress and relevant theories and techniques needed in modelling the sensor/actuator system are reviewed in Chapter 2. A one dimensional sensor model is established in Chapter 3, and the effects of the bonding layer properties on the dynamic electromechanical behavior of the sensor system are discussed. A modified actuator model is established in Chapter 4, and the effects of the bonding layer properties on the dynamic behaviour of the actuator system are studied. Finally, the conclusions and contributions of this thesis are summarized in Chapter 5, and perspective topics are suggested for future studies.

Chapter 2

Literature Review

2.1 Piezoelectricity and Piezoelectric Ceramics

Piezoelectricity is the ability of materials to generate surface charges in response to applied mechanical strain. Direct piezoelectric effect was firstly demonstrated by the brothers Pierre Curie and Jacques Curie in 1880. The converse effect, that is, the production of stress and strain when an electric field is applied, was theoretically predicted by Gabriel Lippmann based on thermodynamic principles in 1881. The Curies immediately confirmed the existence of the converse effect, and obtained quantitative proof of the complete reversibility later on. For the next few decades, more works were done to explore and define the crystal structures that can exhibit piezoelectricity.

The first practical application of piezoelectric devices was the development of an ultrasonic submarine detector by Paul Langevin in France in 1917. This detector consisted of a transducer, which was made by thin quartz crystals carefully glued between two steel plates. This transducer was used to generate acoustic waves to locate submerged objects. Later on, significant efforts had been made in the development of new piezoelectric devices [10, 11, 12].

During the World War II, a new class of man-made materials, ferroelectrics,

were discovered. Ferroelectrics are a class of piezoelectric materials that exhibit a spontaneous polarization under an applied electric field [13]. This discovery led to further development of piezoelectric ceramics with specific properties for particular applications. The first piezoelectric ceramic material, barium titanate (BaTiO3), was discovered independently by researchers in the United States, Japan, and the Soviet Union in 1943 [14]. It remained the primary electroceramic material until the discovery of lead zirconate titanate (PZT) in 1954 [15, 16]. Compared with natural piezoelectric crystals, these newly discovered and developed piezoelectric ceramics are more versatile with physical, chemical and piezoelectric characteristics, and can be tailored for specific applications. Due to their superior coupling effects between electric and mechanical fields, piezoelectric ceramics have been widely used in electromechanical devices, such as actuators, sensors and transducers [17].

The use of piezoelectric ceramic materials as sensors and actuators in SHM systems has been considerably increased during the past few decades [18]-[22]. Compared with conventional transducers, piezoelectric sensors and actuators are small, thin and unobtrusive. They can be easily shaped and put into small spaces, or built inside of structures; they are low in cost, so they can be installed in sensor arrays to cover large surfaces, which could be really expensive if conventional transducers were used.

2.2 Global Response of the Piezoelectric Systems

As a result of the extensive use of piezoelectric patches in SHM systems, significant attentions have been paid to the studies of the global response of piezoelectric systems [23]-[26]. Simplified sensor/actuator models have been established to simulate the sensing or actuation process of embedded and surface-bonded

piezoelectric patches. A simply-supported beam model with a pair of out-of-phase surface-bonded piezoelectric actuators is established to study the beam response when it is excited in bending by the actuators at resonance frequencies [27]. The coupling between the bending, axial and torsional vibrations of composite beams with surface-bonded piezoelectric sensor layers has been studied theoretically [28]. A sandwich beam embedded with a piezoelectric actuator layer is studied for the flexural analysis of the piezoelectric structure using the Bernoulli-Euler beam model [29]. In this model, the distribution of the piezoelectric potential along the longitudinal direction of the actuator is obtained by enforcing the Maxwell equation. Results show that the dynamic characteristics of the entire structure is related to the position of the piezoelectric layer. Besides, the mode shape distribution of the electric potential inside the piezoelectric layer along the longitudinal direction is related to the curvature of the sandwich beam, and depends on the boundary conditions.

The use of piezoelectric patches in structural shape control has also been investigated by many researchers [30, 31, 32]. In the early studies, the shape control of fiber-reinforced composite beams, plates and shells by using embedded piezoelectric actuators is investigated [33, 34]. Analytical methods are developed in these studies to determine the necessary input voltages in order to achieve specific shapes of the structures. To further study the optimal actuator voltage needed to attain a desired shape of structures, a finite element model of laminated composite beams with integrated piezoelectric actuators is developed [35]. In this study, a higher order shear deformation theory and lateral strains are considered in formulating the governing equations. The shape control and damage identification of a cantilever composite beam are studied in [36]. Results show that the position and extension of damages of the beam

can be determined by measuring its static response. A composite laminated beam model with surface-bonded piezoelectric actuators is established to study nonlinearity of the piezoelectric patches and its effects on the shape control of beams [37]. Finite element procedure is used to solve the governing coupled nonlinear constitutive equations, and results indicate the importance of considering the nonlinearity of the material in order to improve the performance of piezoelectric actuators.

2.3 Electromechanical Impedance Techniques

Electromechanical impedance (EMI) approach is suitable for near field structural damage detection. The mechanism of the EMI method is to employ structural excitations through surface-bonded piezoelectric patches and to monitor the changes in the impedance of the structure. This method is especially effective at ultrasonic frequencies, which provide a high sensitivity to the changes in local dynamics due to incipient structural damage. In the last ten years, extensive effects have been made to promote the development of this technique.

In early studies of the EMI method, an electromechanical model is established to give a quantitative description of the process of the impedance method [38]. The results show that, the electrical impedance of the piezoelectric patches is directly related to the mechanical impedance of the host structure, thus demonstrating the feasibility of using EMI method for structural damage detection. Subsequently, this method has been used by many researchers for health monitoring of different types of structures. Damage detection of an assembled truss structure by employing this method is studied [39]. Later, this method is used to implement the real-time damage evaluation of a large and massive bridge joint, and the feasibility of EMI method on

damage detection of large civil infrastructures is proved [40]. This method has also been used for typical civil facilities such as steel bridge joints and pipeline systems [41, 42]. The most important observation in [42] is that this method can tolerate mechanical noise, thus can be used to detect imminent damage of civil facilities, such as unburied pipeline systems, under normal operating conditions and immediately after a natural disaster. The results also show a promising potential for the health monitoring of buried pipelines. Novel ways of interpreting the EMI spectra and identifying structural damages have been further explored [43, 44, 45].

2.4 Elastic Wave Propagation in Piezoelectric Systems

The use of piezoelectric patches for damage detection of structures based on elastic wave propagation has attracted significant attention [46, 47, 48]. Elastic waves are sensitive to the changes of geometry and parameters of the material, and can propagate over a long distance in a structure. Therefore, they are attractive for the quick, large range inspection of structures. They also have the potential to detect both surface cracks and embedded damage. Due to these advantages, comparing with other methods for damage detection, such as using electromagnetic field and thermal field [49], elastic waves have been more widely used in active SHM systems [50, 51, 52, 53].

Theoretical and experimental study of the elastic wave generation and detection by using piezoceramic patches has been conducted [54]. In this work, numerical results based on the finite element simulation of piezoelectric actuators and sensors in generating and detecting elastic waves are presented. The potential application of using interdigital electrodes to generate and detect elastic waves in piezoelectric structures is further discussed. Extensive

works have been done to study the use of piezoelectric patches for inducing and receiving elastic waves to conduct health monitoring of different structures [55, 56, 57]. A set of experiments are presented in which both the EMI technique and the wave propagation approach are used for damage detection [58]. Experiment results indicate that these two techniques are complementary and need to be used simultaneously in order to ensure the complete coverage of the monitored structures. The concept of using a continuous sensor for detecting vibration and stress waves in a uniform cantilever bar is studied [59]. Experiment results show that the damage in the bar can be detected by recognizable changes in the sensor output. Besides, this continuous sensor can also be replaced by four or more individual sensors.

However, the major difficulties of using elastic waves to conduct structural health monitoring are that the signals are not instinctually interpretable due to the complicated behaviour of elastic waves, such as the dispersive characteristics of the waves, the presence of multi-modes, and the existence of complicated mode conversions [60, 61]. These difficulties lead to further studies about the interaction between host structures and incorporated piezoelectric sensors/actuaters, and the resulting complicated electromechanical behaviour in a smart SHM system [62, 63].

2.5 The Local Stress Field Around Piezoelectric Patches

Due to the presence of material discontinuity between the sensors/actuators and the host structures, a complicated local electromechanical field is generated near the edges of the the sensors/actuators. This requires a detailed understanding of the local stress field around piezoelectric patches. Recently, many efforts have been made in this area [5]-[9].

A cantilever beam model with embedded and surface-bonded thin sheet piezoelectric actuators is established to study the load transfer between the actuators and the host beam [64]. In this study, the axial stress along the actuator is assumed to be uniformly distributed across the thickness of the actuator, and the host structure was modelled as a Bernoulli-Euler beam. Later, this model is modified by considering the linear strain distribution along the thickness of the actuators [65]. The actuator model in [64] has been further modified to study the response of a beam with piezoelectric actuator under general loadings. Both the axial and the transverse shear force are considered in formulating the governing equations [66].

A one dimensional model is developed recently to study the static and dynamic electromechanical behaviour of piezoceramic actuators attached to an elastic insulator when the system is subjected to in-plane mechanical and electrical loads [67]. The influences of different coefficients are investigated to show the effects of the geometry of the actuators, the material combination and the loading frequency upon the load transfer between the actuators and the host structure. The interaction between different actuators is also studied by using a pseudo-incident wave method. This actuator model is also used to study the generation of Rayleigh wave for monitoring surface damage of structures using a single actuator and multiple actuators [68]. This actuator model is further modified to study problems with varying electric field distribution along the actuators [69], with the effect of both the longitudinal and the transverse deformations of the actuators being considered.

Similar to this actuator model, a one dimensional sensor model is established to study the relation between the sensor response and the deformation of the host medium under static and dynamic loads [70]. Results indicate the

significant effect of the geometry of the sensor, the material mismatch of the system, and loading frequency upon the sensor response.

2.6 Studies on the Bonding Layers in Low Frequency Cases

In these studies reviewed so far, the sensors/actuators are assumed to be perfectly bonded to the host structures, and the effect of the bonding layer is ignored. However, since the modulus of the bonding layer is usually lower than that of the sensors/actuators and the host structures, it may significantly affect the local stress field distribution. Recently, several studies have reported that the controllability of smart structures can suffer when the mechanical properties of the bonding layer are ignored in the dynamic model of smart structures [71, 72]. This means, a more complete control model can be obtained if the mechanical properties of the bonding layer have been considered [73]. The vibration properties of composite beams with attached sensors and actuators are investigated for three different adhesives [73]. The optimal-type adhesives are chosen based on their contribution to the controllability of the cantilevered beams.

A bending-extensional dynamic model of a simply-supported beam with attached piezoelements is proposed [74]. In this study, the shear bonding layers both for the actuator and for the sensor are assumed visco-elastic, which are described by the Kelvin-Voigt model. The influence of the bonding layer parameters on the active damping response of the controlled beam under a low frequency harmonic concentrated force is analyzed. The results show that the stiffness of bonding layer affects significantly the active damping efficiency. A

three dimensional sensor model, which is later simplified into a two dimensional one, is established [75]. In this model, the bonding medium is considered as an elastic layer, with a finite stiffness in the thickness direction. Considerable thickness comparable to the thickness of the piezoelectric sensor is assumed. The effect of the shear stress in the bonding layer on the sensing effectiveness of piezoelectric patches is studied. This investigation addresses the phenomena that the strain drops sharply near the edges and shows that end-bonding must be carefully assessed in order to enhance the quality of the sensing output.

Unlike the cases in vibration control problems, in structural damage detection problems, high frequency elastic waves with wavelength comparable to the size of actuators/sensors are commonly generated inside the structures. However, the effects of the bonding condition on the dynamic behaviour of the sensors/actuators in high frequency cases have not been thoroughly studied.

2.7 Summary

We have reviewed existing studies on piezoelectric sensor/actuator systems. The bonding condition does show its significant influence on the dynamic behaviour of the system. However, little attention has been paid to the cases under high loading frequency. Therefore, the current work aims at providing a comprehensive theoretical study on the effects of the bonding condition on the dynamic behaviour of the piezoelectric sensors/actuators, and the focus will be given to high frequency cases.

Chapter 3

Analysis of the Piezoelectric Sensor system

This chapter provides a comprehensive study of the influence of material parameters of the bonding layer on the coupled electromechanical characteristics of piezoelectric sensors, which are subjected to high frequency mechanical loads. A one dimensional sensor model with a bonding layer, which undergoes a shear deformation, is proposed. Analytical solutions based on the use of the integral equation method are provided. Detailed numerical simulation is conducted to evaluate the effect of the bonding layer under different loading frequencies. To consider the effect of the electrodes at the upper and lower surfaces of the sensor, the output voltage of the sensor is further studied.

3.1 Formulation of the Problem

The considered system is a homogeneous and isotropic elastic medium, with a piezoceramic sensor surface-bonded to it. Between the medium and the sensor, there is a thin bonding layer, as illustrated in Figure 3.1. The lengths of both the sensor and the bonding layer are denoted as $2a$, and the thicknesses of the sensor and the bonding layer are denoted as h and h', respectively. In Figure 3.1, z axis is the poling direction of the sensor, in which electric field is

usually applied or measured. The system is subjected to a harmonic incident longitudinal wave with a frequency of ω and angle of θ_0. The displacement of the incident wave is given by

$$\overline{u} = A_0 \cdot \exp\left[i(ky\sin\theta_0 + kz\cos\theta_0 - \omega t)\right] \tag{3.1}$$

where A_0 denotes the magnitude of the displacement, and $k = \omega/c_L$ is the wave number, with c_L being the longitudinal wave speed.

The steady state response of the system, including displacement, stress, and strain, will involve a time factor $\exp(-i\omega t)$. For example, the real displacement can be expressed as:

$$\overline{u} = u(y,z) \cdot \exp\left(-i\omega t\right) \tag{3.2}$$

where $\overline{u}$ represents the real displacement field, and u represents the magnitude. Since $\exp(-i\omega t)$ exists in all parameters, for the purpose of convenience, in the following discussions, only the magnitude of these field variables are used to represent these field variables.

This study will focus on a thin-sheet sensor, with relatively small thickness in comparison with its length. Therefore, the magnitude of axial stress σ_y^s and strain ε_y^s can be assumed to be uniform across the thickness of the sensor, where the superscript 's' represents sensor. Since the thickness of the bonding layer is usually smaller than that of the sensor, the same assumption is used for the bonding layer. The interfacial shear stress distributed in the bonding layer is denoted as τ, which also represents the shear stress between different layers, as shown in Figure 3.2. The displacements on the upper and lower surface of the bonding layer are denoted as u^+ and u^-, respectively. u^+ and

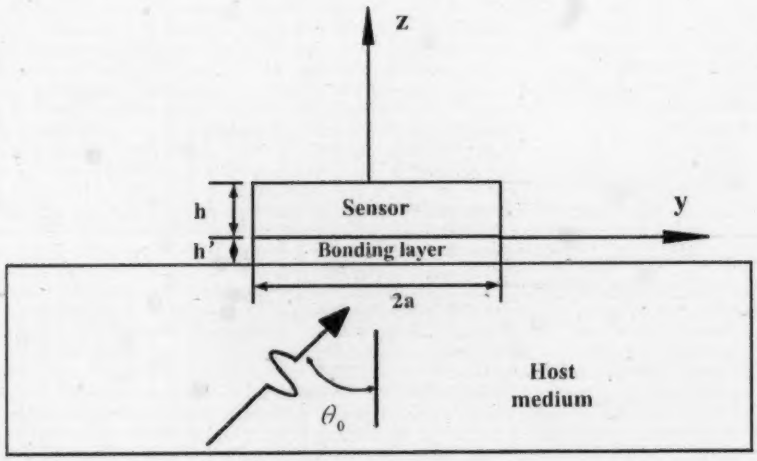

Figure 3.1: Geometry of the sensor system

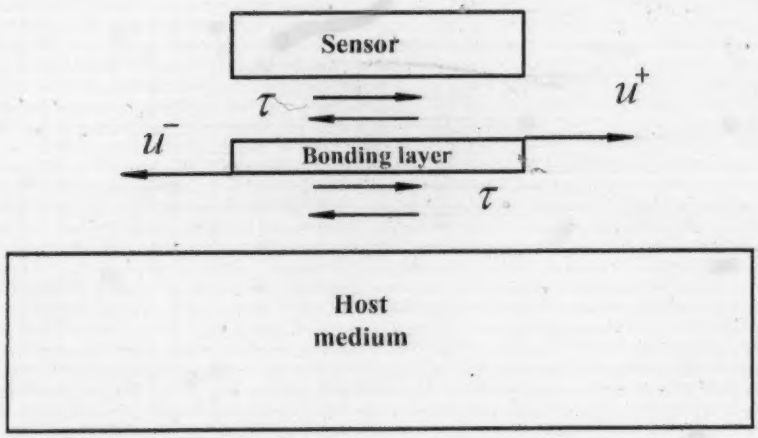

Figure 3.2: Stress fields of the sensor system

u^- also represent the displacements at the bottom of the sensor layer and the displacement on the top of the host medium, respectively.

3.1.1 Modelling of the Bonding Layer

The bonding layer is the connection between the sensor and the host structure. Its shear modulus, thickness, and coefficient of viscosity, will determine the property of the layer. Since the modulus of the layer is normally lower than that of the sensor and the host structure, the layer may have significant effect upon the load transfer between the sensor and host structure.

The real shear stress $\overline{\tau}$ distributed in the layer is determined by the constitutive relation:

$$-\overline{\tau} = \mu_b \overline{\varepsilon}_y + c_b \dot{\overline{\varepsilon}}_y \tag{3.3}$$

where

$$\overline{\tau} = \tau \exp(-i\omega t) \tag{3.4}$$

$$\overline{\varepsilon}_y = \frac{u^+ - u^-}{h'} \exp(-i\omega t) \tag{3.5}$$

$$\dot{\overline{\varepsilon}}_y = \frac{\partial[(\frac{u^+ - u^-}{h'}) \exp(-i\omega t)]}{\partial t} \tag{3.6}$$

with the subscript 'b' representing the bonding layer, μ_b and c_b being the shear modulus and the coefficient of viscosity of the bonding layer, respectively. τ is the magnitude of the shear stress distributed in the layer; $\overline{\varepsilon}_y$ is the real longitudinal strain of the bonding layer; u^+ and u^- are the longitudinal displacements of the upper and lower bonding layer surface, respectively.

In Equation (3.2), u is not a function of time. Therefore, Equation (3.6)

can be reduced to

$$\dot{\varepsilon}_y = (-i\omega)\frac{u^+ - u^-}{h'}\exp(-i\omega t). \tag{3.7}$$

Therefore, by substituting Equation (3.7) into Equation (3.3), and by eliminating the time factor $\exp(-i\omega t)$ on both sides, Equation (3.3) can be rewritten as:

$$-\tau = (\frac{\mu_b}{h'} - \frac{i\omega c_b}{h'})(u^+ - u^-). \tag{3.8}$$

As we mentioned before, u^+ and u^- also denote the longitudinal displacements of the lower surface of the sensor layer and the upper surface of the host medium, respectively. Therefore, their expression can be obtained by analyzing the dynamic behaviours of the sensor and the host medium.

3.1.2 The Dynamic Sensor Model

3.1.2.1 Electromechanical Behaviour of Piezoelectric Materials

The electromechanical behaviour of piezoelectric materials can be described as [76]

$$\{\sigma\} = [c]\{\varepsilon\} - [e]\{E\}, \quad \{D\} = [e]\{\varepsilon\} + [\lambda]\{E\} \tag{3.9}$$

where $\{\sigma\}$, $\{\varepsilon\}$, $\{D\}$ and $\{E\}$ represent the magnitude of the stresses, the strains, the electric displacement and the electric field intensity, respectively. $[c]$ is a matrix containing the elastic stiffness parameters for a constant electric potential, $[e]$ represents the piezoelectric constants, and $[\lambda]$ represents the dielectric constants for zero strains.

Plane strain deformation in y-z plane will be considered in the current study, which suggests that $\varepsilon_x = 0$. For a surface-bonded piezoelectric thin sheet with the direction of its length is defined as y-axis, the traction-free condition along its surface suggests that $\sigma_z = 0$. Therefore, following condition should be satisfied,

$$\varepsilon_x = 0, \quad \sigma_z = 0. \tag{3.10}$$

The stress component σ_y and electric displacement D_z can be obtained by substituting the above equation into the constitutive equation, and the results are as follows:

$$\sigma_y = (c_{11} - \frac{c_{13}^2}{c_{33}})\varepsilon_y - (e_{13} - e_{33}\frac{c_{13}}{c_{33}})E_z \tag{3.11}$$

$$D_z = (e_{13} - e_{33}\frac{c_{13}}{c_{33}})\varepsilon_y + (\lambda_{33} + \frac{e_{33}^2}{c_{33}})E_z \tag{3.12}$$

where c_{11}, c_{13} and c_{33} are the elements of $[c]$, e_{13} and e_{33} are the elements of $[e]$, and λ_{33} is the element of $[\lambda]$.

Therefore, the constitutive relation of the piezoelectric material under plane strain deformation is given by

$$\sigma_y = E\frac{\partial u_y}{\partial y} - eE_z \tag{3.13}$$

$$D_z = e\frac{\partial u_y}{\partial y} + \lambda E_z \tag{3.14}$$

with

$$\varepsilon_y = \frac{\partial u_y}{\partial y}. \tag{3.15}$$

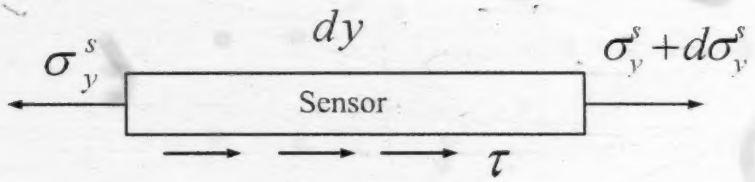

Figure 3.3: Stress field inside of the sensor

The effective material constants of the piezoelectric materials can be expressed as

$$\begin{aligned} E &= c_{11} - \frac{c_{13}^2}{c_{33}} \quad \textit{plane strain} \\ e &= e_{13} - e_{33}\frac{c_{13}}{c_{33}} \quad \textit{plane strain} \\ \lambda &= \lambda_{33} + \frac{e_{33}^2}{c_{33}} \quad \textit{plane strain.} \end{aligned} \tag{3.16}$$

3.1.2.2 The current sensor model

The current study focuses on the case when the system is subjected to a high-frequency mechanical field, which generates wave propagation with a wave length comparable to the length of the sensor. As a result, the inertia effect of the sensor must be considered [70]. According to the stress field shown in Figure 3.3, the equation of motion of the sensor can be expressed as:

$$\frac{d\overline{\sigma}_y^s}{dy} + \frac{\overline{\tau}(y)}{h} = \rho_s \frac{\partial^2 \overline{u}_y^s}{\partial^2 t} \tag{3.17}$$

where the superscript and subscript 's' represent sensor, ρ_s is the mass density of the sensor, and $\overline{\sigma}_y^s$ represents the real axial stress along the the sensor.

From the expression of $\overline{u}$ in Equation (3.2), it can be obtained that:

$$\frac{\partial^2 \overline{u}_y^s}{\partial^2 t} = -\omega^2 u_y^s \exp(-i\omega t) \tag{3.18}$$

where u_y^s represents the magnitude of the axial displacement along the sensor. By using the above result and by eliminating the time factor on both sides of Equation (3.17), Equation (3.17) now becomes:

$$\frac{d\sigma_y^s}{dy} + \tau(y)/h + \rho_s \omega^2 u_y^s = 0 \tag{3.19}$$

where σ_y^s represents the magnitude of the axial stress along the the sensor.

Since there is no external force applied at the two ends of the sensor, traction free boundary condition can be applied as follows:

$$\sigma_y^s = 0, \quad |y| = a. \tag{3.20}$$

In addition, the sensor will operate in an open-loop mode with no external charge supplied to it [77]. Therefore, the electric displacement across the sensor will be zero, as

$$D_z = 0. \tag{3.21}$$

By using Equation (3.13), Equation (3.14) and Equation (3.21), σ_y^s can be expressed as follows:

$$\sigma_y^s = (E_s + \frac{e_s^2}{\lambda_s}) \frac{\partial u_y^s}{\partial y} \tag{3.22}$$

where E_s, e_s and λ_s are piezoelectric material parameters defined in Equation

(3.16).

By substituting Equation (3.22) into Equation (3.19), the governing equation of the sensor can be rewritten as

$$(E_s + \frac{e_s^2}{\lambda_s})\frac{\partial^2 u_y^s}{\partial y^2} + p(y) + \rho_s \omega^2 u_y^s = 0 \tag{3.23}$$

where

$$p(y) = \frac{\tau(y)}{h}. \tag{3.24}$$

For the sensor, define an effective modulus

$$\overline{E}_s = E_s + \frac{e_s^2}{\lambda_s}, \tag{3.25}$$

and a wave number

$$k_s = \frac{\omega}{c_s} \tag{3.26}$$

where the axial wave speed c_s is given by

$$c_s = \sqrt{\overline{E}_s/\rho_s}. \tag{3.27}$$

Equation (3.23) can be rewritten as

$$\frac{\partial^2 u_y^s}{\partial y^2} + k_s^2 u_y^s + \frac{p(y)}{\overline{E}_s} = 0. \tag{3.28}$$

The solution of Equation (3.28) is

$$u_y^s = A_0 \cos k_s y + B_0 \sin k_s y - \frac{1}{k_s \overline{E}_s} \int_{-a}^{y} p(\xi) sin[k_s(y-\xi)] d\xi, \quad |y| < a \quad (3.29)$$

where A_0 and B_0 are constants. By using the traction free boundary condition defined in Equation (3.20), A_0 and B_0 can be obtained

$$\begin{cases} A_0 = -\dfrac{1}{2k_s \overline{E}_s \sin k_s a} \displaystyle\int_{-a}^{a} p(\xi) \cos[k_s(a-\xi)] d\xi \\ \\ B_0 = \dfrac{1}{2k_s \overline{E}_s \cos k_s a} \displaystyle\int_{-a}^{a} p(\xi) \cos[k_s(a-\xi)] d\xi. \end{cases} \quad (3.30)$$

Then the longitudinal displacement of the sensor in Equation (3.29) can be expressed as:

$$\begin{aligned} u_y^s(y) = &-\frac{\cos[k_s(a+y)]}{k_s \overline{E}_s \sin 2k_s a} \int_{-a}^{a} \cos[k_s(\xi - a)] p(\xi) d\xi \\ &-\frac{1}{k_s \overline{E}_s} \int_{-a}^{y} \sin[k_s(y-\xi)] p(\xi) d\xi \quad |y| < a. \end{aligned} \quad (3.31)$$

3.1.3 Dynamic Behaviour of the Host Medium

The dynamic plane strain displacement field in a homogeneous isotropic elastic medium is governed by [79],

$$u_y = \frac{\partial \Phi}{\partial y} + \frac{\partial \Psi}{\partial z}, \qquad u_z = \frac{\partial \Phi}{\partial z} - \frac{\partial \Psi}{\partial y} \quad (3.32)$$

where Φ and Ψ are two displacement potentials which satisfy

$$(\nabla^2 + K^2)\Phi = 0, \qquad (\nabla^2 + k^2)\Psi = 0 \quad (3.33)$$

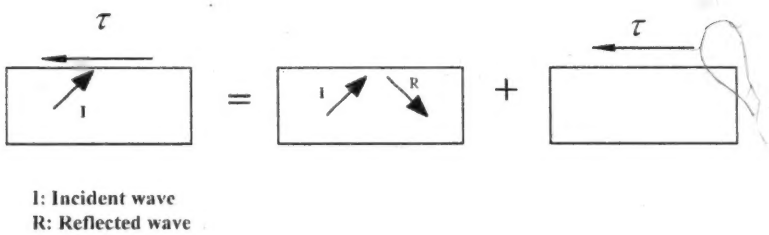

Figure 3.4: The stress field inside of the host medium-sensor system

in which the Laplace operator ∇^2 stands for $\frac{\partial^2}{\partial y^2} + \frac{\partial^2}{\partial z^2}$ and K and k are two wave numbers defined as

$$K = \omega/c_L, \quad k = \omega/c_T \tag{3.34}$$

with c_L and c_T being the longitudinal and transverse shear wave speed of the elastic medium, respectively.

The stress field generated inside of the host medium can be divided into two parts, as shown in Figure 3.4. Once the incident longitudinal wave reaches the upper surface of the host medium, it will be reflected. By using Equations (13)-(19) introduced in Appendix A, the first part of the displacement of the medium can be obtained, and recorded as u_y^I. The second part of the displacement, denoted as u_y^τ, is due to the shear stress τ on the top surface of the medium.

The general solution of the wave induced by τ can be determined by solving the governing equations using the following Fourier transform

$$f^*(s) = \frac{1}{2\pi}\int_{-\infty}^{\infty} f(y)e^{isy}dy, \quad f(y) = \int_{-\infty}^{\infty} f^*(s)e^{-isy}ds. \tag{3.35}$$

Therefore, the solution can be expressed as

$$\Phi^*(s,y) = A(s)e^{\alpha z}, \quad \Psi^*(s,y) = B(s)e^{\beta z} \tag{3.36}$$

from which the displacement components can be determined as

$$u_y^* = -isA(s)e^{\alpha z} + \beta B(s)e^{\beta z} \tag{3.37}$$

$$u_z^* = \alpha A(s)e^{\alpha z} + isB(s)e^{\beta z} \tag{3.38}$$

where $(^*)$ represents Fourier transform. $A(s)$ and $B(s)$ are two unknown functions of s, and α and β are given by

$$\alpha = \begin{cases} \sqrt{s^2 - K^2} & |\mathrm{s}|>\mathrm{K} \\ -i\sqrt{K^2 - s^2} & |\mathrm{s}|<\mathrm{K} \end{cases} \qquad \beta = \begin{cases} \sqrt{s^2 - k^2} & |\mathrm{s}|>\mathrm{k} \\ -i\sqrt{k^2 - s^2} & |\mathrm{s}|<\mathrm{k} \end{cases} \tag{3.39}$$

which ensure that the induced stress field satisfies the radiation condition of the problem.

By making use of the general solution of u_y^* and u_z^*, the expression of stress field σ_{yz}^* and σ_z^* can be obtained

$$\begin{cases} \sigma_{yz}^*(y,z) = \mu_h[2\dfrac{\partial^2\Phi^*}{\partial y\partial z} - k^2\Psi^* - 2\dfrac{\partial^2\Psi^*}{\partial y^2}] \\ \qquad\qquad = -2i\mu_h s\alpha A(s)e^{\alpha z} + \mu_h(2s^2 - k^2)B(s)e^{\beta z} \\ \sigma_z^*(y,z) = \mu_h[-2\dfrac{\partial^2\Phi^*}{\partial y^2} - k^2\Phi^* - 2\dfrac{\partial^2\Psi^*}{\partial y\partial z}] \\ \qquad\qquad = \mu_h(2s^2 - k^2)A(s)e^{\alpha z} + 2i\mu_h s\beta B(s)e^{\beta z} \end{cases} \tag{3.40}$$

where the subscript 'h' represents the host medium, and μ_h is the shear modulus of the matrix.

At the top surface of the host structure, where $z = 0$, the stress field becomes

$$\begin{cases} \sigma^*_{yz}(y,0) = -2i\mu_h s\alpha A(s) + \mu_h(2s^2 - k^2)B(s) \\ \\ \sigma^*_z(y,0) = \mu_h(2s^2 - k^2)A(s) + 2i\mu_h s\beta B(s). \end{cases} \tag{3.41}$$

By using the following boundary condition

$$\begin{cases} \sigma_{yz}(y,0) = -\tau, \qquad |y| < a, \\ \sigma_z(y,0) = 0 \end{cases} \tag{3.42}$$

$A(s)$ and $B(s)$ can be solved as follow:

$$\begin{cases} A(s) = \dfrac{2is\beta}{\mu_h[(2s^2 - k^2)^2 - 4s^2\alpha\beta]}\tau^*(s) \\ B(s) = -\dfrac{2s^2 - k^2}{\mu_h[(2s^2 - k^2)^2 - 4s^2\alpha\beta]}\tau^*(s) \end{cases} \tag{3.43}$$

where

$$\tau^*(s) = \frac{1}{2\pi}\int_{-a}^{a} \tau(\xi)e^{is\xi}d\xi. \tag{3.44}$$

Therefore, the dynamic displacement $u_y^{\tau^*}$ can be determined as

$$u_y^{\tau^*}(y,0) = \frac{\beta k^2}{\mu_h[(2s^2 - k^2)^2 - 4s^2\alpha\beta]}\tau^*(s). \tag{3.45}$$

By using the inverse Fourier Transform, u_y^τ can be obtained as

$$u_y^\tau(y,0) = \frac{1}{2\pi\mu_h}\int_{-\infty}^{\infty}\frac{\beta k^2}{(2s^2-k^2)^2-4s^2\alpha\beta}\int_{-a}^{a}\tau(\xi)e^{-is(y-\xi)}d\xi ds$$
$$= \frac{1}{\pi\mu_h}\int_0^{\infty}\frac{\beta k^2}{(2s^2-k^2)^2-4s^2\alpha\beta}\int_{-a}^{a}\tau(\xi)\cos[s(y-\xi)]d\xi ds. \quad (3.46)$$

It can be observed that the property of the kernel of the integration when $s \to \infty$ represents the singular behaviour of the field,

$$\frac{\beta k^2}{(2s^2-k^2)^2-4s^2\alpha\beta} \to -\frac{\lambda_0}{2s}sgn(s), \quad as \quad s \to \infty \quad (3.47)$$
$$sgn(s) = 1, \quad when \quad 0 < s \quad (3.48)$$

where $\lambda_0 = 2(1-\nu_h)$ with ν_h being the Poisson's ratio.

Equation (3.46) can be expressed as

$$u_y^\tau(y,0) = -\frac{\lambda_0}{2\pi\mu_h}\int_0^{\infty}\frac{sgn(s)}{s}\int_{-a}^{a}\tau(\xi)\cos[s(y-\xi)]d\xi ds$$
$$+\frac{1}{\pi\mu_h}\int_0^{\infty}[\frac{\beta k^2}{(2s^2-k^2)^2-4s^2\alpha\beta}+\frac{\lambda_0}{2s}]\int_{-a}^{a}\tau(\xi)\cos[s(y-\xi)]d\xi ds. \quad (3.49)$$

Since

$$\int_0^{\infty}sgn(s)\sin[s(y-\xi)]ds = \frac{1}{y-\xi}, \quad (3.50)$$

the first term of the right hand side of Equation (3.49) becomes

$$-\frac{\lambda_0}{2\pi\mu_h}\int_0^{\infty}\frac{sgn(s)}{s}\int_{-a}^{a}\tau(\xi)\cos[s(y-\xi)]d\xi ds$$
$$= \int_{-a}^{y}\frac{\lambda_0}{2\pi\mu_h}\int_0^{\infty}sgn(s)\int_{-a}^{a}\tau(\xi)sin[s(y-\xi)]dsd\xi dy$$
$$= \frac{\lambda_0}{2\pi\mu_h}\int_{-a}^{y}\int_{-a}^{a}\tau(\xi)\frac{1}{y-\xi}d\xi dy \quad (3.51)$$

Thus, the resulting dynamic displacement along the interface between the bonding layer and the host medium can be determined as

$$u_y^h(y,0) = \frac{1}{\pi\mu_h}\int_0^\infty [\frac{\beta k^2}{(2s^2-k^2)^2-4s^2\alpha\beta}+\frac{\lambda_0}{2s}]\int_{-a}^{a}\tau(\xi)\cos[s(y-\xi)]d\xi ds + \frac{\lambda_0}{2\pi\mu_h}\int_{-a}^{y}\int_{-a}^{a}\tau(\xi)\frac{1}{y-\xi}d\xi dy + u_y^I, |y|<a. \quad (3.52)$$

where the superscript and subscript 'h' represent the host medium.

3.1.4 Dynamic Load Transfer

By substituting Equations (3.31) and (3.52) into Equation (3.8), Equation (3.8) can be rewritten as

$$-\frac{\cos[k_s(a+y)]}{k_s\overline{E}_s\sin 2k_sa}\int_{-a}^{a}\cos[k_s(\xi-a)]p(\xi)d\xi - \frac{1}{k_s\overline{E}_s}\int_{-a}^{y}\sin[k_s(y-\xi)]p(\xi)d\xi - \frac{1}{\pi\mu_h}\int_0^\infty [\frac{\beta k^2}{(2s^2-k^2)^2-4s^2\alpha\beta}+\frac{\lambda_0}{2s}]\int_{-a}^{a}\tau(\xi)\cos[s(y-\xi)]d\xi ds - \frac{\lambda_0}{2\pi\mu_h}\int_{-a}^{y}\int_{-a}^{a}\tau(\xi)\frac{1}{y-\xi}d\xi dy + \frac{h'}{\mu_b-i\omega c_b}\tau(y) = u_y^I(y), \quad |y|<a \quad (3.53)$$

The general solution of Equation (3.53) can be expressed in terms of the first kind of Chebyshev polynomials, T_j, as

$$\tau(y) = \sum_{j=0}^{\infty} c_j T_j(y/a)/\sqrt{1-y^2/a^2} \quad (3.54)$$

where

$$T_j(y/a) = \cos(j\theta), \quad \cos\theta = y/a \quad (3.55)$$

If τ is expanded into N terms, and Equation (3.53) is satisfied at the following locations along the sensor

$$y = a\cos[\frac{l}{N+1}\pi], \quad l = 1, 2, \cdots, N, \quad |y| < a \tag{3.56}$$

Equation (3.53) becomes N linear algebraic equations in term of $\{c\} = \{c_0, c_1, \cdots, c_{N-1}\}^T$, the coefficients of Chebyshev expansion. These N equations can be written in the form of:

$$[Q^s]\{c\} = \{F^s\} \tag{3.57}$$

where $[Q^s]$ is the resulting known matrix, and $\{F^s\}$ is the applied load matrix, whose expression are given as follow:

$$\begin{aligned} Q^s_{lj} = & \frac{\overline{h'}}{(\mu_b - i\omega c_b)} \cdot \frac{T_j(\eta^l)}{\sqrt{1-\eta^{l2}}} - \pi \frac{\cos[\overline{k}_s(1+\eta^l)]}{\overline{k}_s \overline{E}_s \overline{h} \sin(2\overline{k}_s)} P_j^2 \\ & + \frac{1}{\overline{k}_s \overline{E}_s \overline{h}} \int_{\cos^{-1}\eta^l}^{\pi} \sin([\overline{k}_s(\cos\theta - \eta^l)]\cos(j\theta) d\theta \\ & - \frac{1}{\mu_h} \int_0^{\infty} P_j^1 \left(\frac{\overline{\beta k}^2}{[(2\overline{s}^2 - \overline{k}^2)^2 - 4\overline{s}^2\overline{\alpha}\overline{\beta}]} + \frac{\lambda_0}{2\overline{s}}\right) d\overline{s} + \frac{\lambda_0}{2\mu_h} P_j^3 \end{aligned} \tag{3.58}$$

and

$$\{F^s\} = u_y^I(\eta^l, 0) \tag{3.59}$$

where

$$\eta^l = y^l/a, \quad \overline{k} = ka, \quad \overline{k}_s = k_s a, \quad \overline{s} = sa. \tag{3.60}$$

The parameters P_j^1, P_j^2 and P_j^3 in Equation 3.58 are given by

$$\begin{aligned} P_j^1 &= J_j(\bar{s}) \begin{cases} (-1)^n \sin(\bar{s}\eta^l) & j = 2n+1 \\ (-1)^n \cos(\bar{s}\eta^l) & j = 2n \end{cases} \\ P_j^2 &= J_j(\bar{k}_s) \begin{cases} (-1)^n \sin(\bar{k}_s) & j = 2n+1 \\ (-1)^n \cos(\bar{k}_s) & j = 2n \end{cases} \\ P_j^3 &= \begin{cases} \frac{[\cos(j\cos^{-1}\eta^l) - (-1)^j]}{j} & j \neq 0 \\ 0 & j = 0 \end{cases} \end{aligned} \tag{3.61}$$

with J_j $(j = 1, 2\cdots)$ and T_j being the Bessel functions of the first kind and the Chebyshev polynomials, respectively.

By solving Equation (3.57), $\{c\}$ can be obtained. It can then be used to determine the axial displacement u_y^s and the axial strain ε_y^s of the sensor, by using the following two equations:

$$\begin{cases} u_y^s = [Q_1^s]\{c\} \\ \\ \varepsilon_y^s = [Q_2^s]\{c\} \end{cases} \tag{3.62}$$

where

$$\begin{cases} [Q_1^s] = -\pi \dfrac{\cos[\bar{k}_s(1+\eta^l)]}{\bar{k}_s \bar{E}_s \bar{h} \sin(2\bar{k}_s)} P_j^2 + \dfrac{1}{\bar{k}_s \bar{E}_s \bar{h}} \displaystyle\int_{\cos^{-1}\eta^l}^{\pi} \sin([\bar{k}_s(\cos\theta - \eta^l)]\cos(j\theta)d\theta \\ \\ [Q_2^s] = \pi \dfrac{\sin[\bar{k}_s(1+\eta^l)]}{\bar{E}_s \bar{h} \sin(2\bar{k}_s)} P_j^2 - \dfrac{1}{\bar{E}_s \bar{h}} \displaystyle\int_{\cos^{-1}\eta^l}^{\pi} \cos([\bar{k}_s(\cos\theta - \eta^l)]\cos(j\theta)d\theta. \end{cases} \tag{3.63}$$

3.2 Results and Discussion

In this section, a longitudinal wave will be introduced as the mechanical load, and numerical simulation for special cases will be conducted. Since the strain distribution along the sensor is a reflection of the load transfer between the sensor and the host medium, attention will be focused on it. The effect of material properties of the bonding layer, the loading frequency, the material combination, and the sensor geometry upon the load transfer will be studied.

Different material combination of the sensor and host structure can be represented by the material mismatch factor q, which is defined as follow:

$$q = \frac{\pi E_h}{2(1-\nu_h^2)\bar{E}_s}. \tag{3.64}$$

The sensor geometry parameter, denoted as v, is defined as the ratio of the sensor length to its thickness:

$$v = \frac{a}{h} \tag{3.65}$$

where a and h are the length and thickness of the sensor, respectively.

The material constants of the typical piezoceramic (PZT) sensor are shown in Table 3.1[78]; the material parameters of the host medium and the bonding layer are shown in Table 3.2[70]. The material constant of the bonding layer is assumed based on the existing material constant [73]. The mass densities of the sensor and the host medium, ρ_s and ρ_h, are chosen of the same value as $2700Kg/m^3$. The geometry of the sensor and the bonding layer are as follow: a=1cm, $h = 0.5mm$, and the range of h'/a is from 0 to 0.032, where a, h, and h' are the length of the sensor, the thickness of the sensor, and the thickness of

Table 3.1: Material Properties of the PZT Sensor/Actuator

Elastic Stiffness Parameters	c_{11}	c_{12}	c_{13}
(Pa)	13.9×10^{10}	6.78×10^{10}	7.43×10^{10}
Piezoelectric Constants	e_{31}	e_{33}	e_{15}
(C/m^2)	-5.2	15.1	12.7
Dielectric Constants	λ_{11}	λ_{22}	λ_{33}
(C/Vm)	6.45×10^{-9}	6.45×10^{-9}	5.62×10^{-9}

Table 3.2: Material Properties of the Host Medium and the Bonding Layer-Sensor System

Host medium	
Young's Modulus E_h (Pa)	2.74×10^{10}
Poisson's Ratio ν_h	0.3
Bonding Layer	
Shear Modulus μ_b (Pa)	1.0×10^9

the bonding layer, respectively. Based on the current selection of the material combination, the material mismatch parameter $q = 0.3928$, and the sensor geometry parameter $v = 20.0$.

3.2.1 Wave Propagation Inside the Host Medium

The waveforms of the incident P-wave as well as the reflected P-wave and S-wave are given in Equation (1) in Appendix A. As defined in Equation (1), k represents the wave number of the incident wave. A normalized wave number ka is used to represent the loading frequency. In the current simulation, k is selected as the wave number of P-wave, and $ka = 1.0$ means the loading frequency is $0.11MHz$. The angle of the incident wave θ_0 is selected as 30^0, and the range of loading frequency ka is selected from 1.0 to 20.0. Employing Equations (13) to (19), the displacement on the top surface of the host medium,

u^I, as $\overrightarrow{U}$ in Equation (19) in Appendix A, can be determined. By using Equation (3.57), the Chebychev coefficients can be solved. The coefficients can then be used in Equation (3.62) to determine the displacement and strain field along the sensor.

3.2.2 Strain Distribution Along the Sensor

If the sensor does not exist, the incident wave will generate a strain distribution along the top surface of the host medium $\varepsilon_y^I(y)$. With the sensor, the strain will be disturbed and the strain field along the sensor is denoted as $\varepsilon_y^s(y)$. The dynamic strain ratio, $\kappa(y)$, is defined as:

$$\kappa(y) = \frac{\varepsilon_y^s(y)}{\varepsilon_y^I(y)} = Ae^{i\theta}, \quad |y/a| < 1 \tag{3.66}$$

where A and θ denote the amplitude and phase angle of the dynamic strain ratio.

The amplitude of the dynamic strain ratio, A, represents the percentage of deformation transferred from the host medium to the sensor. It is an index of the sensing characteristics of the piezoelectric sensor. In this section, attention will be focused on the dynamic strain distribution represented by A. The effect of different material properties of the bonding layer and the sensor, and the loading frequency upon it will be discussed.

3.2.2.1 The Effect of the Thickness of the Bonding Layer

Equation (3.8) indicates that, the combination of μ_b and h', μ_b/h', is the major parameter that represents the stiffness of the bonding layer. It can be observed that, μ_b and h' contribute to the stiffness through μ_b/h'. The increase of μ_b

value can result in a stiffer bonding layer, and so does the decrease of the h' value. Because of their similar contribution to the load transfer, for the convenience of discussion, in this part of study, μ_b value is fixed to a constant, and h' is changed to achieve different bonding layer stiffness.

To investigate the deformation transfer between the sensor and the host medium, the thickness of the bonding layer is selected as a serial of $h' = 0$, 10, 40, 80, 160 and 320 μm. The coefficient of viscosity c_b is selected as 10 $Pa \cdot s$, which corresponds to very weak viscosity. Three loading frequencies, $ka = 1.0$, 4.0, and 8.0, are selected, and the corresponding amplitudes of the dynamic strain ratio curves are shown in Figures 3.5 to Figure 3.7, respectively.

In Figure 3.5, the horizontal axis represents the position along the sensor. In other words, $y/a = 0$ denotes the center of the sensor; while $y/a = \pm 1$ denotes the two ends of the sensor. As the results displayed in Figure 3.5, these six curves are similar in shape. With the increase of the thickness of the bonding layer from 0 to 320 μm, the amplitude of the curve drops, from 0.8 to 0.6.

The curves in Figure 3.6, however, begin to show changes in their shapes. When the sensor is perfectly bonded, two peaks appear in the strain distribution curve. As the thickness of the bonding layer increases up to 80 μm, the amplitude of these peaks decreases. If the thickness continues to increase to $h' = 160$ or 320 μm, only one peak appears in the curve, and its amplitude increases with the increase of the thickness.

More significant changes in shapes are displayed in Figure 3.7. When h' is between 0 and 80 μm, only one major peak appears in each curve, which is around y/a =0.6. With the increase of h', up to 80, the amplitude of the peak increases as well, and the rest of the curve becomes relatively flat. When

$h' = 160$, two peaks are observed in the strain distribution curve, with the amplitude around 1.4 and 2.6, respectively. And if h' goes to 320 μm, three peaks appear, with significant drops in the amplitude.

The results obtained in Figure 3.5, Figure 3.6 and Figure 3.7 indicate that, the thickness of the bonding layer affects the amplitude of the strain distribution curve more significantly in relatively high frequency cases.

The phase angle of the dynamic strain ratio curves for $ka = 1.0$, 4.0, and 8.0 are shown in Figure 3.8, 3.9 and 3.10, respectively, for different bonding layer thicknesses.

When the loading frequency is relatively low, as shown in Figure 3.8, for $ka = 1.0$, the phase angle difference between the results for different layer thicknesses is insignificant. However, with the increase of the frequency, the phase angle shows more dependence on the bonding layer thickness, as shown in Figure 3.9 and Figure 3.10. For $ka = 8.0$, Figure 3.10, difference in phase angle of the dynamic strain ratio as high as 180^0 can be observed. The result indicates that, the effect of the thickness of the bonding layer on the phase angle of the dynamic strain ratio curve is more significant for relatively high frequency cases than for relatively low frequency ones.

3.2.2.2 The Effect of the Coefficient of Viscosity of the Bonding Layer

From Equation (3.8), it can be observed that, as another parameter of the stiffness of the bonding layer, the coefficient of viscosity also contributes to the load transfer between the sensor and the host medium. But it appears as an imaginary value in the equation. It should be mentioned that, since $\exp(-i\omega t)$ has been eliminated from all the parameters, imaginary part of a parameter will effect both the amplitude and the phase angle. In order to

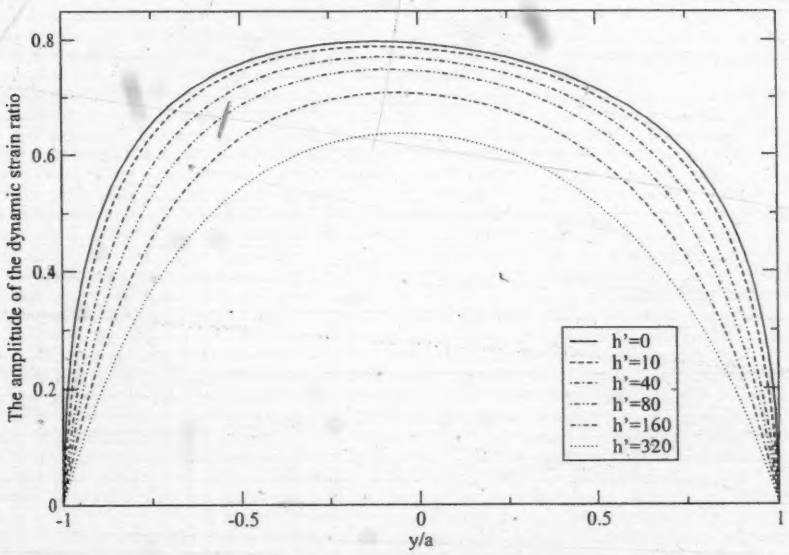

Figure 3.5: Normalized strain distribution along the sensor (ka=1.0, q=0.3928, v=20.0, $c_b = 10$).

study its effect on the load transfer, $h' = 100\mu m$ is used and a serial of c_b value is selected, from 10 to 10000. $c_b = 10Pa \cdot s$ represents very weak viscosity; while $c_b = 10000Pa \cdot s$ represents strong viscosity. The loading frequency is chosen as $ka = 1.0$, and the results of the distribution of the amplitude of the dynamic strain ratio along the sensor are shown in Figure 3.11.

As shown in Figure 3.11, the curve doesn't change much when c_b is increased from 10 to 1000 $Pa \cdot s$. As c_b continue to increase, changes in the amplitude becomes more and more obvious. When $c_b = 10000$ $Pa \cdot s$, the amplitude of the strain distribution along the sensor of the curve is pretty close to that of the first curve in Figure 3.5, which is for the case where the system is under perfect bonding condition ($h' = 0$). In other words, the increase of the viscosity of the bonding layer contributes in a similar way to the load transfer as the decrease

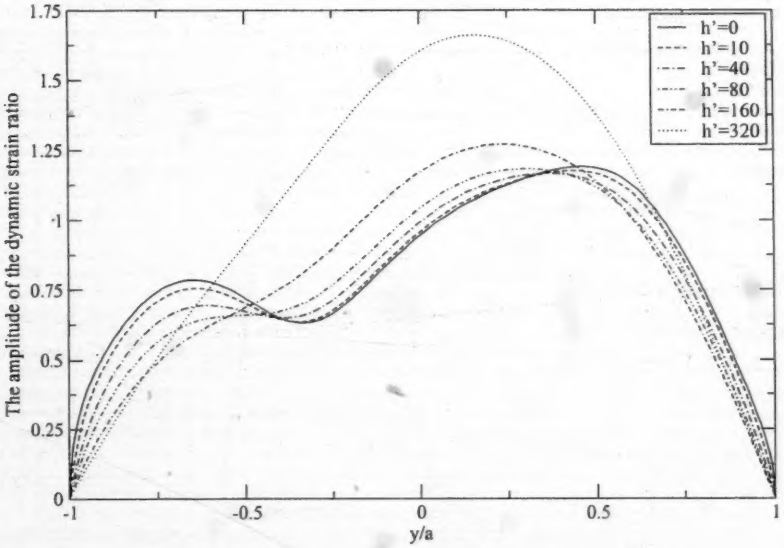

Figure 3.6: Normalized strain distribution along the sensor (ka=4.0, q=0.3928, v=20.0, $c_b = 10$)

of its thickness or the increase of the modulus.

3.2.2.3 The Effect of the loading frequency

As the results shown in Figure 3.5, Figure 3.6, and Figure 3.7, the loading frequency has significant influence on the load transfer between the sensor and the host structure. To take a closer look, two bonding conditions $h' = 0$ and $h' = 100\mu m$ are considered, and a serial of ka values, ka = 1.0, 2.0, 4.0, 8.0, 12.0 and 16.0 is chosen to investigate how the strain distribution varies with different loading frequencies. The corresponding dynamic strain ratio curves are shown in Figure 3.12 and Figure 3.13, respectively.

As shown in Figure 3.12, the shape of the strain distribution curves change significantly with the increase of the loading frequency. When ka=1.0, the

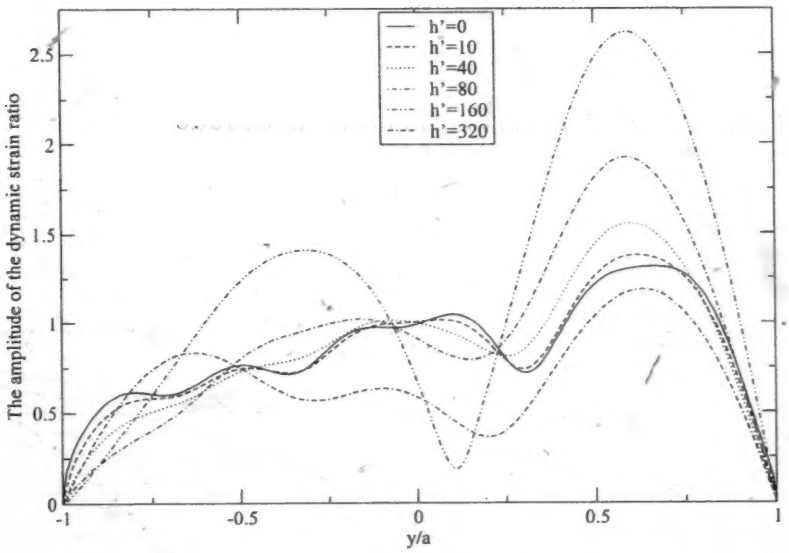

Figure 3.7: Normalized strain distribution along the sensor (ka=8.0, q=0.3928, v=20.0, $c_b = 10$)

curve is flat in the internal region of the sensor, with the amplitude of the curve around 0.8. As ka value gets higher, more peaks appear in the curve, and at the same time, the maximum peak value gets higher. When $ka = 16.0$, four major peaks are observed in the curve, with the maximum peak value around 1.5.

When a bonding layer ($h' = 100\mu m$) is included, significant changes of the shape of the strain distribution curves with the increase of loading frequency are shown in Figure 3.13. For relatively low frequency $ka = 1.0$ or 2.0, the strain distribution curve has quite similar shape to the corresponding result in Figure 3.12. As ka increases, significant variation of the strain distribution curves is observed, with increasing peak numbers and peak values. This indicates the fact that, with the effect of the bonding layer, the effect of the

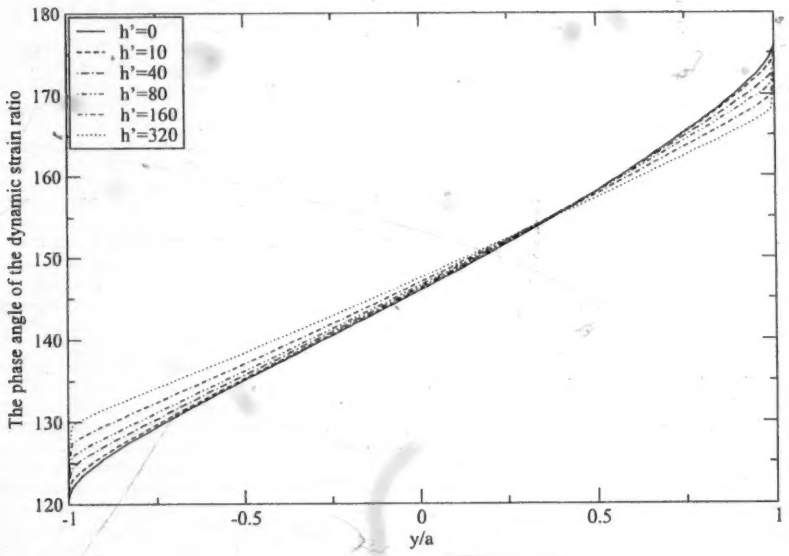

Figure 3.8: The phase angle of the dynamic strain ratio θ^0 (ka=1.0, q=0.3928, v=20.0, $c_b = 10$)

loading frequency upon the load transfer may become more significant.

The results obtained suggest that, when loading frequency is relatively high ($ka > 2.0$, for example), the strain distribution along the sensor might be too complicated to measure. It should be mentioned that $ka = 2.0$ corresponds to a frequency of $0.22MHz$.

3.2.2.4 The Effect of the Material Combination

As defined in Equation (3.64), q is an index of the relative stiffness of the sensor, representing the material mismatch between the sensor and the host medium. In our calculation, the material constants of the sensor are fixed; while the Young's Modulus of the host medium is adjusted to achieve different q values. In previous examples, the selection of sensor and host medium results

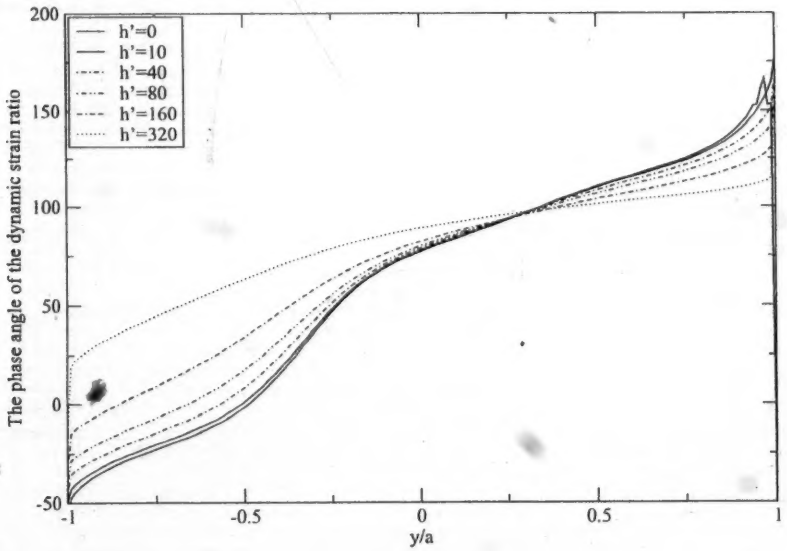

Figure 3.9: The phase angle of the dynamic strain ratio θ^0 (ka=4.0, q=0.3928, v=20.0, $c_b = 10$)

in $q = 0.3928$. For the convenience of calculation, $q = 0.1$, 0.5, 1.0, 2.0, 5.0 are selected. Two bonding conditions, $h' = 0$ and $100\mu m$ are considered, and the loading frequency $ka = 1.0$ are selected to study the effect of material combination upon the load transfer. The results are shown in Figure 3.14 and Figure 3.15, respectively.

Figure 3.14 shows how the strain distribution along the sensor changes with the decrease of the relative stiffness of the sensor, when the system is under perfect bonding condition ($h' = 0$). With the decrease of the stiffness of the sensor, the amplitude of the dynamic strain ratio distribution curve increases. When the stiffness of the sensor reaches 5.0, the strain distribution curve becomes very flat, approaching 1.0, because the disturbance of a softer sensor is relatively insignificant.

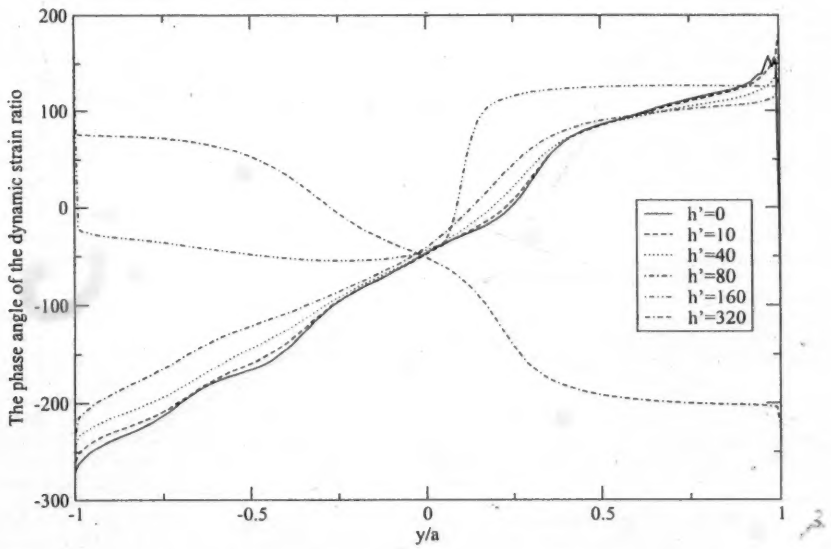

Figure 3.10: The phase angle of the dynamic strain ratio θ^0 (ka=8.0, q=0.3928, v=20.0, $c_b = 10$)

The corresponding result for the case where the bonding condition is not perfect, $h' = 100\mu m$, is shown in Figure 3.15. In this case, the thickness is selected to be $100\mu m$, and the loading frequency remains the same, $ka = 1.0$. Again, significant effect of the material mismatch q is observed. In comparison with the results shown in Figure 3.14, the amplitude changes between two consecutive curves are more obvious. Although when q equals 2.0, the amplitude of the distribution curve is around 1.0, as q value continues to increase, the maximum value of the curve can reach 1.25. Considering the fact that higher q value corresponding to softer sensor, the current result indicates that, even when the host structure is much stiffer than the sensor, the effect of the bonding layer on the load transfer will still be very important.

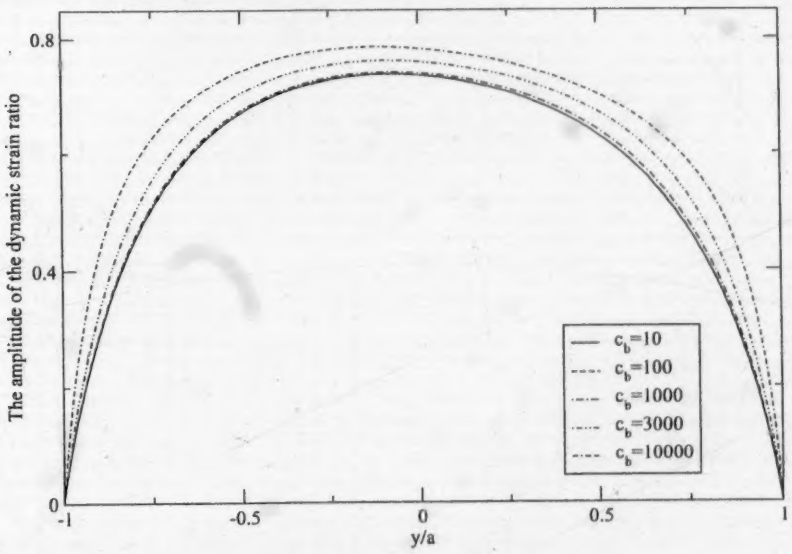

Figure 3.11: Normalized strain distribution with different coefficients of viscosity ($ka = 1.0$, $h' = 100$, $q = 0.3928$, $v = 20.0$)

3.2.2.5 The Effect of the Geometry of the Sensor

The geometry of the sensor also shows its influence on the dynamic behavior of the sensor. In this study, the sensor geometry is represented by the length-to-thickness ratio v, which is defined in Equation (3.65). To investigate its effect on the dynamic behaviour of the sensor, a serial v value, $v = 5.0$, 10.0, 15.0 and 20.0, is selected. Two bonding conditions, $h' = 0$ and $h' = 100\mu m$ are considered, and $ka = 1.0$ is chosen as the loading frequency.

The result for a perfectly bonded sensor ($h' = 0$) is shown in Figure 3.16 for different length-to-thickness ratios. In this case, the length of the sensor is fixed. With the increase of the v value (decrease of h), the amplitude of the curve increases dramatically. This value when v=20.0 is approximately twice as much as that of the curve when v=5.0. This clearly shows that thinner

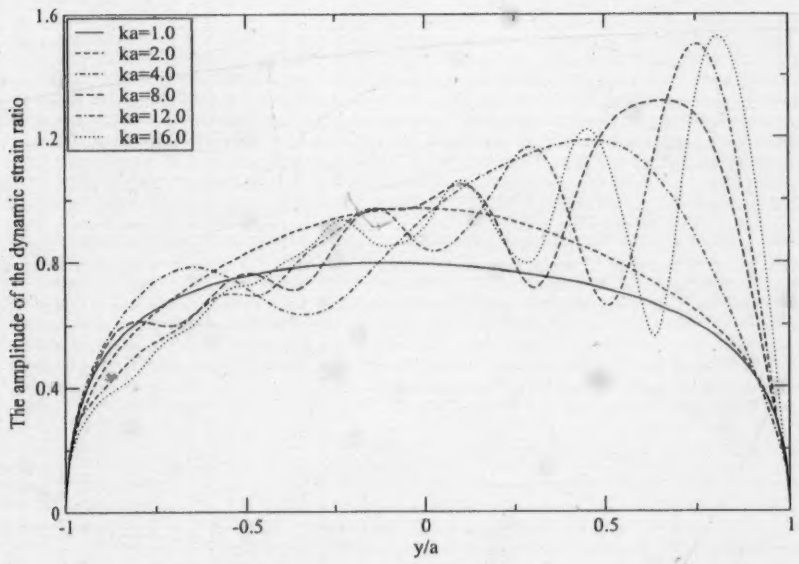

Figure 3.12: Normalized strain distribution with different loading frequencies ($h' = 0, q = 0.3928, v = 20.0$)

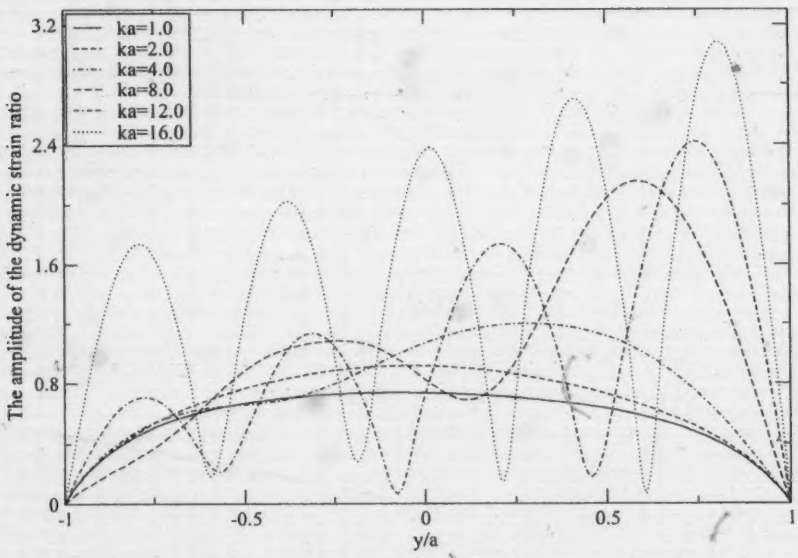

Figure 3.13: Normalized strain distribution with different loading frequencies ($h' = 100$, $q = 0.3928$, $v = 20.0$, $c_b = 10$)

sensor will experience a strain ratio closer to one.

Similar trend is observed in Figure 3.17, when bonding layer effect is involved. The amplitude of each strain distribution curve is smaller than its corresponding one in Figure 3.16. This indicates that the change of the sensor geometry does not respond to the mechanical field changes as much as it does when the bonding condition is perfect.

3.2.3 Output Voltage of the Sensor

Since the sensor operates in an open-loop mode with no external charges applied to it, as indicated in Equation (3.21), the electric field intensity, E_z,

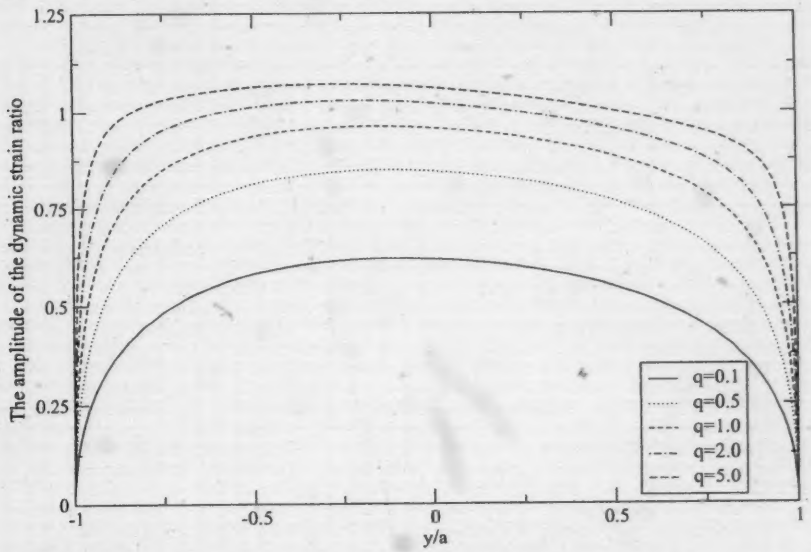

Figure 3.14: Normalized strain distribution along the sensor with different material combinations (ka=1.0, h'=0, v=20.0)

defined in Equation (3.14) can be expressed as follow:

$$E_z(y) = -\frac{e_s}{\lambda_s}\frac{\partial u_y^s}{\partial y}. \tag{3.67}$$

According to the relationship between voltage and electric field intensity, the voltage distribution along the sensor can be determined as

$$V(y) = -\int_0^h E_z(y)dz = \frac{e_s h}{\lambda_s}\frac{\partial u_y^s}{\partial y}. \tag{3.68}$$

When the upper and lower surfaces of the sensor form two electrodes, the total resulting voltage across the sensor can be obtained by averaging the

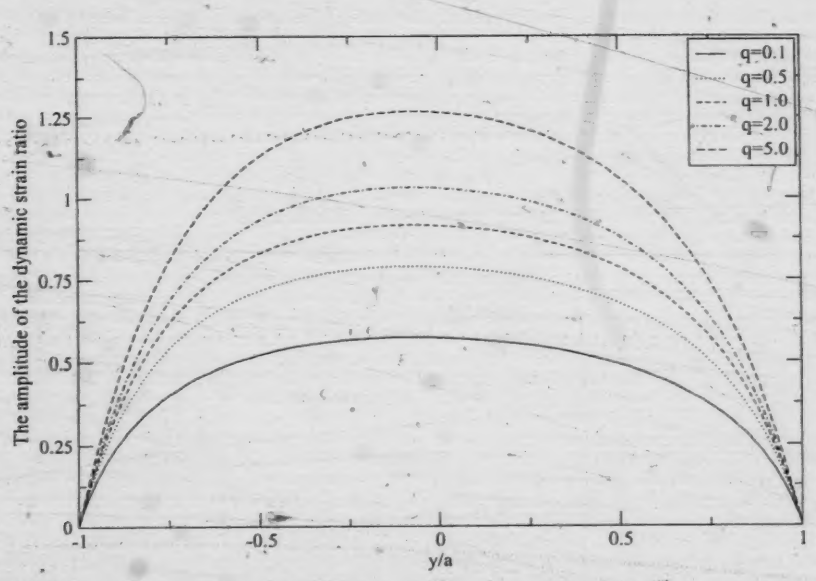

Figure 3.15: Normalized strain distribution along the sensor with different material combinations (ka=1.0, h'=100, v=20.0, c_b=10)

voltage across the sensor obtained before, i.e.

$$V^{out} = \frac{1}{2a}\int_{-a}^{a} V(y)dy = \frac{e_s h}{2a\lambda_s}|u_y^s(a) - u_y^s(-a)|. \tag{3.69}$$

V^{out} is an important parameter of the piezoelectric sensor, which will be measured in a real system. The higher the V^{out} value, the stronger the signal detected by the sensor is. The focus of this section will be on V^{out}. Studies will be conducted to investigate how V^{out} value varies with different bonding conditions, loading frequencies, material combinations and sensor geometries.

3.2.3.1 The Effect of the Thickness of the Bonding Layer

As we discussed before, since the shear modulus of the bonding layer, μ_b, contributes to the load transfer in a 'similar' way as the thickness of the bonding

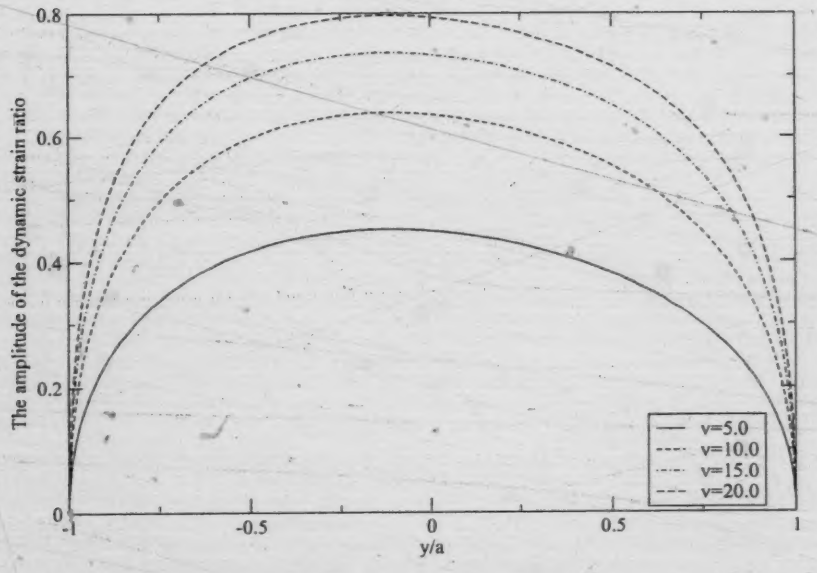

Figure 3.16: Normalized strain distribution along the sensor with different sensor geometries (ka=1.0, h'=0, q=0.3928)

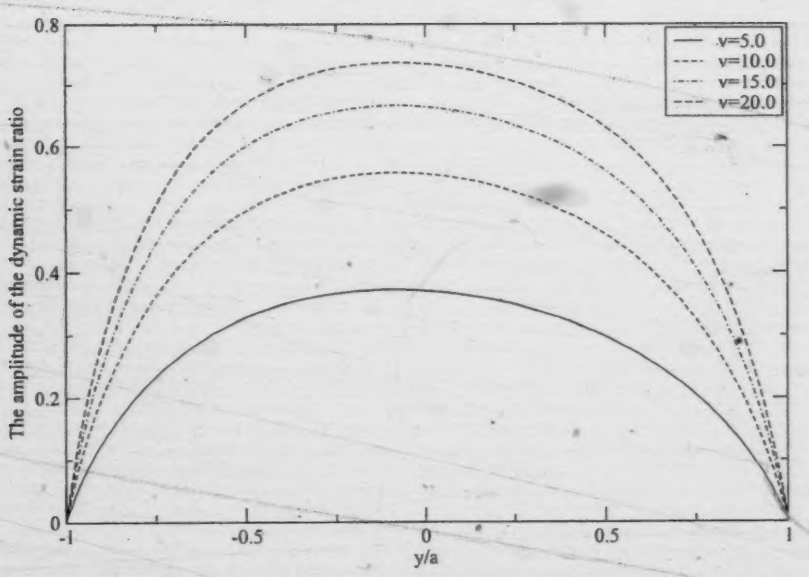

Figure 3.17: Normalized strain distribution along the sensor with different sensor geometries (ka=1.0, h'=100, q=0.3928, c_b=10)

layer does, in this part of the study, the shear modulus is fixed, and only the thickness of the bonding layer is changed to achieve different stiffness of the bonding layer. A serial of the thickness of the bonding layer, $h' = 0$, $20\mu m$, $40\mu m$, ... $320\mu m$, is selected, and loading conditions with ka =1.0, 2.0, 4.0, 8.0, 12.0, 16.0, and 20.0 are chosen to show how the output voltage varies with the increase of thickness of the bonding layer under different loading conditions. In the examples considered here, the amplitude of the incident strain field is kept to be the same and the output voltage is normalized by the corresponding result for the perfectly bonded sensor ($h' = 0$) for $ka = 1.0$.

Figure 3.18 shows the variation of the normalized output voltage of the sensor with the thickness of the bonding layer under different frequencies. For relatively low loading frequencies, $ka = 1.0$ or 2.0, the effect of layer thickness becomes significant only when the layer gets relatively thick ($h' > 200\mu m$). For relatively high loading frequencies ($ka = 8.0 \sim 20.0$), however, even a thin layer has generated significant effect on the normalized output voltage of the sensor.

3.2.3.2 The Effect of the Material Combination

The relative stiffness of the sensor q is another factor influencing the output voltage of the sensor. $q = 0.1$, 0.5, 1.0, and 5.0 are selected and two bonding conditions, $h' = 0$ and 100 μm are considered to investigate how the output voltage changes with the increase of loading frequency ka from 1.0 to 20.0. The output voltages are normalized by the result obtained when $ka = 1.0$, $h' = 0$, $q = 0.3928$ and $v = 20.0$. The results under two different bonding conditions, $h' = 0$ and $h' = 100\mu m$, are shown in Figure 3.19 and Figure 3.20, respectively.

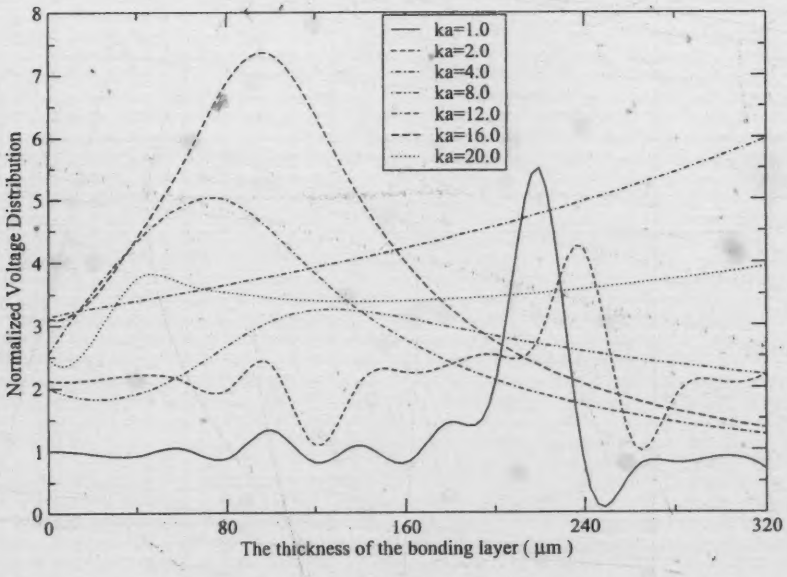

Figure 3.18: Normalized output voltage with different thicknesses of the bonding layer and loading frequencies ($q = 0.3928$, $v = 20.0$, $c_b = 10$)

In Figure 3.19, where $h' = 0$, the shape of each the $V^{out} - ka$ curve does not change much as q value increases from 0.1 to 1.0. Typically three major peaks are observed for all cases considered. As q value reaches 5.0, in addition to the three major peaks, two minor ones appear in the curve.

In Figure 3.20, where $h' = 100\ \mu m$, the $V^{out} - ka$ curves are quite different from previous results given by Figure 3.19, indicating the significant effect of the bonding layer. When $q = 0.1$, the $V^{out} - ka$ curve is relatively flat. When q approaches 0.5, significant changes in the shape of the curve occurs with four peaks being observed in the curve. As q continues to increase to 1.0, one major peak is observed in the curve around $ka = 5.0$. Significant drop in the V^{out} value is observed after ka is increased to 10.0. When $q = 5.0$, significant voltage output is observed for relatively low frequencies ($ka < 2.0$), while the voltage becomes very low when the frequency is high ($ka > 2.0$). The phenomenon observed in Figure 3.20 indicates the fact that, as the thickness of the bonding layer increases, and the stiffness of the sensor decreases, the normalized output voltage drops significantly with the increase of the loading frequencies.

3.2.3.3 The Effect of the Geometry of Sensor

The geometry of sensor not only shows its influence on the dynamic strain distribution, but also on the output voltage of the sensor. Two cases, $h' = 0$ and 100 μm are considered, with v=5.0, 10.0, 15.0 and 20.0 being selected to investigate how the $V^{out} - ka$ curve changes with different sensor geometries. The strain field is kept to be the same, and the output voltage is normalized by the result obtained when $h' = 0$, $ka = 1.0$, $q = 0.3928$ and $v = 20.0$. The results is displayed in Figure 3.21 and Figure 3.22 with two bonding conditions,

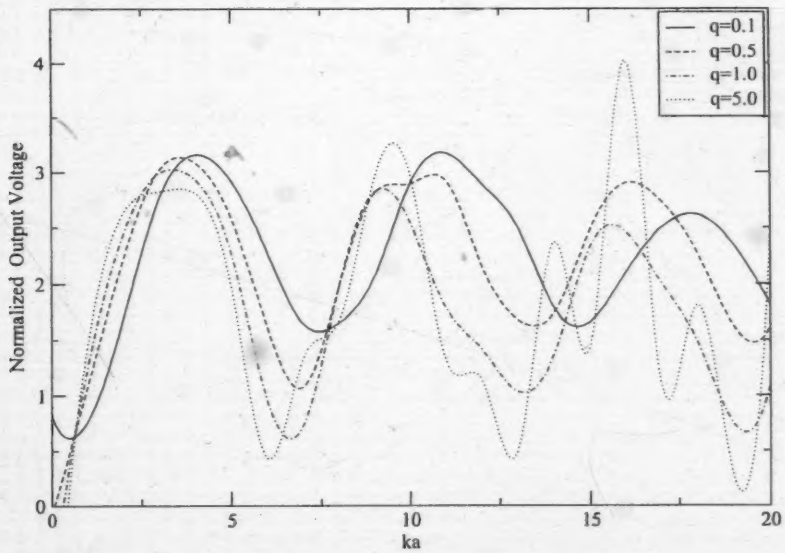

Figure 3.19: Normalized output voltage with different loading frequencies and material combinations ($h' = 0$, $v = 20.0$)

$h' = 0$ and $h' = 100\mu m$, respectively.

In Figure 3.21, when v value decreases from 20.0 to 5.0 (h increases from 0.5 mm to 2.0 mm), the shape of the $V^{out} - ka$ curve does not change much for relatively low frequencies. They almost coincide with one another. As v value drops to 5.0, the three peaks in this curve get sharper in comparison with their corresponding ones in the other three curves, and the location of these peaks are corresponding to lower ka values.

When a bonding layer is included, the phenomenon shown in Figure 3.22 is slightly different from that for perfectly bonded sensors, shown in Figure 3.21. With the decrease of the v value (increase of h value), the amplitude of each peak decreases, and its location moves towards to a lower ka value. This indicates that, with the increase of the thickness of the bonding layer, the

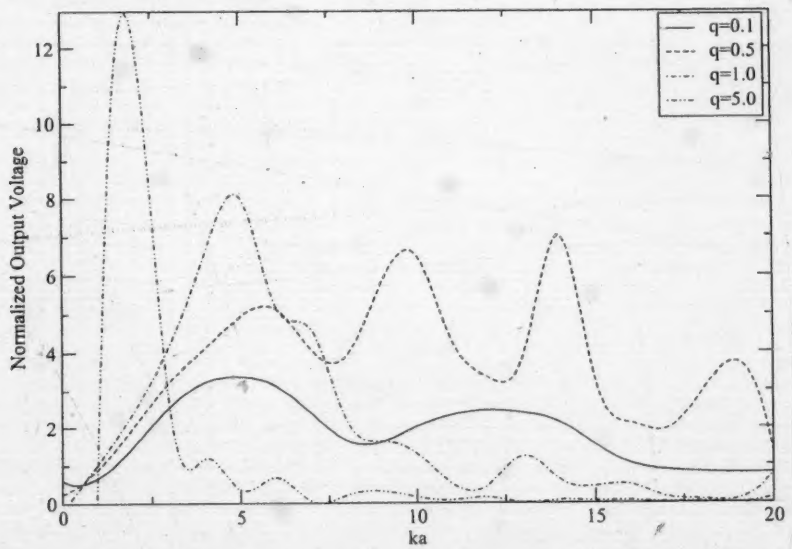

Figure 3.20: Normalized output voltage with different loading frequencies and material combinations ($h' = 100$, $v = 20.0$, $c_b = 10$)

effect of the sensor geometry on the normalized output voltage may become more and more significant.

3.3 Concluding Remarks

The focus of this chapter is on the study of the effect of the material and geometric properties of the sensor and the bonding layer on the load transfer from the host medium to the sensor, when the system is under high frequency mechanical loads. The high frequency discussed in this Chapter starts from $ka = 1.0$, which corresponds to a wave length of the induced elastic wave comparable to the geometry of the sensor. Numerical simulation is conducted for special cases. Specific conclusions are obtained:

(1) The increase of the thickness or decrease of the modulus and viscosity

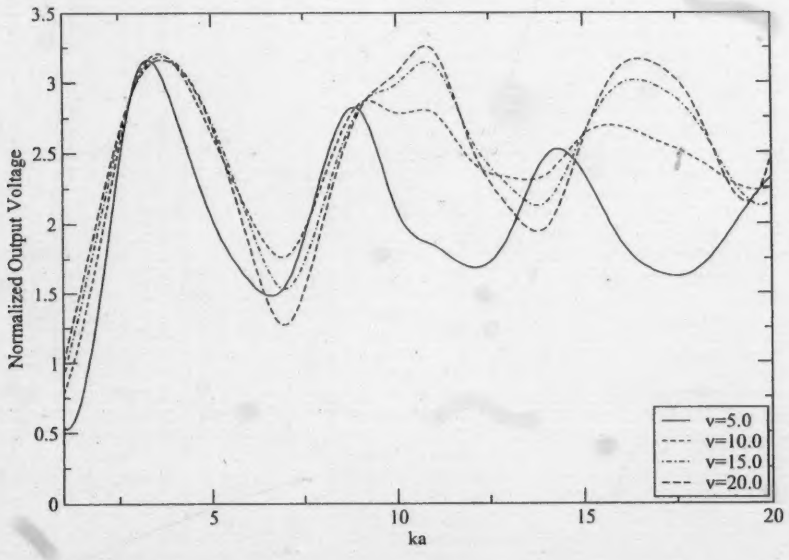

Figure 3.21: Normalized output voltage with different loading frequencies and sensor geometries ($h' = 0$, $q = 0.3928$)

of the bonding layer will reduce the stiffness of the bonding layer. For relatively low frequency cases, $ka = 1.0$, with the decrease of bonding layer stiffness, the amplitude of the strain distribution curve along the sensor gets smaller, by up to 20%. In other words, the signal detected by the sensor gets weaker. For relatively high frequency cases, $ka >= 4.0$, the decrease of bonding layer stiffness can result in a significant variation of the strain distribution along the sensor from that obtained by perfectly bonded sensors.

(2) Based on the current simulation, the currently selected sensor is suitable for detecting or measuring incident wave with loading frequency $ka <= 2.0$. When the loading frequency is relatively high, $ka > 2.0$, the normalized output voltage of the sensor varies a lot with the increase

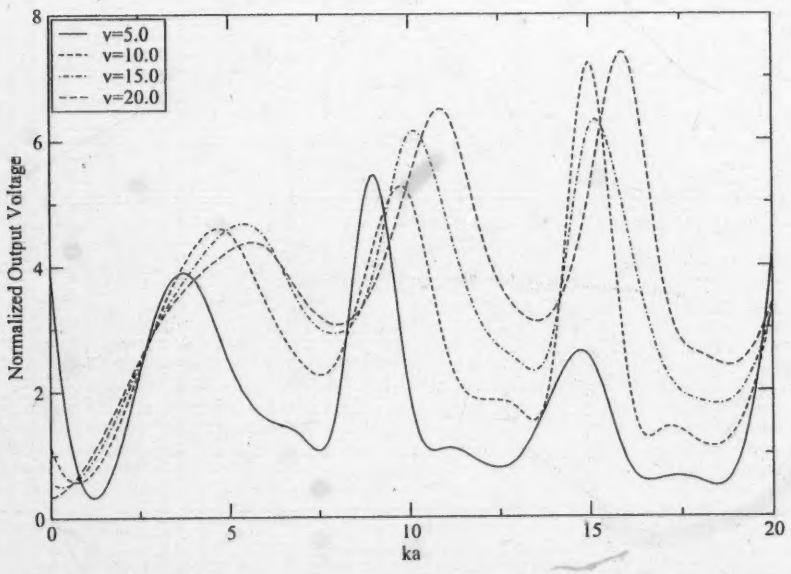

Figure 3.22: Normalized output voltage with different loading frequencies and sensor geometries ($h' = 100$, $q = 0.3928$, $c_b = 10$)

of the bonding layer, even when the bonding layer is relatively thin, $h' < 100\mu m$. This means, the currently selected sensor is not reliable enough to detect the incident wave with loading frequency $ka > 2.0$.

(3) The material combination and sensor geometry show more influence on the normalized output voltage when the bonding condition is not perfect. Based on the current material selection, when the loading frequency is not very high, $ka <= 2.0$, and the thickness of the bonding layer $h' <= 100\mu m$, the material mismatch parameter q between 0.5 and 2.0, and the sensor thickness-to-length ratio in the range of 15.0 to 20.0 are more suitable to select in designing the sensor system, for the strain distribution along the sensor doesn't change too much comparing with that by perfectly bonded condition.

In this Chapter, piezoelectric material is used as a sensor to detect the incident wave, and a better understanding on how the signal collected by the sensor is influenced by the existence of the bonding layer is achieved. The piezoelectric material can also be used as actuator to induce incident wave into the host structure. The property of the actuator also plays an important role in the structural health monitoring process. The effect of the bonding layer on the performance of the actuator will be discussed in Chapter 4.

Chapter 4

Analysis of the Piezoelectric Actuator System

The focus of this Chapter is to study the influence of the bonding layer upon the electromechanical transfer characteristics of the piezoelectric actuator, which is subjected to a high frequency electric field. Similar to the sensor model used in Chapter 3, a one dimensional actuator model with a bonding layer, which undergoes a shear deformation, will be established. Analytical solutions will be deduced and numerical simulation will be conducted for special cases. Attention will be given to material and geometric parameters of the actuator and the host medium, and the loading frequency of the electric field. Their effects on the load transfer from the actuator to the host structure will be studied. Since the actuation is applied to the host medium from the actuator through the interfacial shear stress, attention will be focused on the distribution of shear stress, τ, in the bonding layer. Discussion will include not only the load transfer from the actuator to the host structure, but also the local stress field generated around the actuator, especially around the tips of the actuator.

4.1 Formulation of the Problem

Similar to the sensor model established in Chapter 3, the considered plane strain problem of the actuator can be modelled as a thin piezoelectric sheet surface-bonded to a homogeneous and isotropic elastic insulator. Between the insulator and the actuator is a very thin layer, the bonding layer, as illustrated in Figure 4.1. The lengths of both the actuator and the bonding layer are denoted as $2a$, and the thicknesses of the actuator and the bonding layer are denoted as h and h', respectively. In Figure 4.1, z axis is assumed as the poling direction of the actuator. A voltage is applied between the upper and lower electrodes of the actuator, which results in an electric field $\overline{E}_z$ of frequency ω along the poling direction of the actuator. $\overline{E}_z$ can be expressed as:

$$\overline{E}_z = E_z \exp(-i\omega t) \tag{4.1}$$

where E_z represents the magnitude of the electric field intensity.

Similar to Chapter 3, over bar is used to represent the real parameter containing time variation in forms of $\exp(-i\omega t)$. For the sake of convenience, only the magnitude of these variables are used in the following discussion.

The electric field intensity, E_z, can be obtained by using the following equation:

$$E_z = (V^- - V^+)/h \tag{4.2}$$

where V^- and V^+ represent the electric potential at the lower and upper surface of the actuator.

The present study is focusing on a thin-sheet actuator, with relatively small

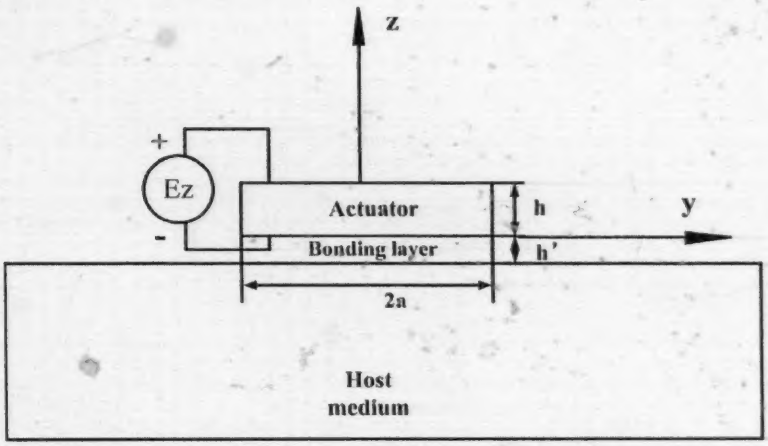

Figure 4.1: Geometry of the actuator system

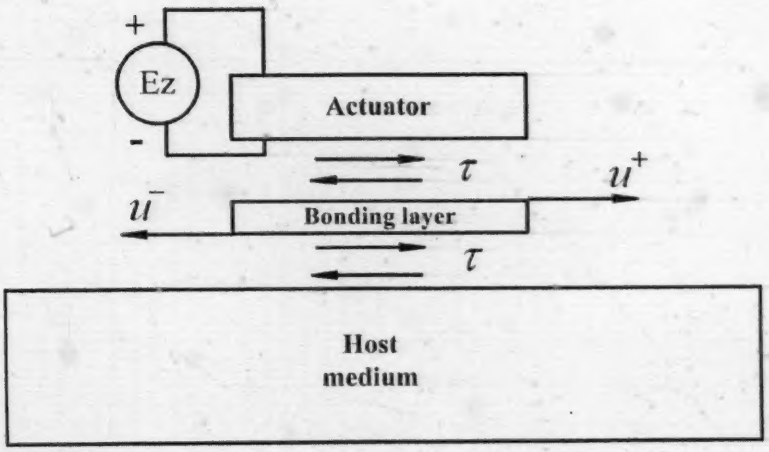

Figure 4.2: Stress fields of the actuator system

thickness in comparison with its length. Therefore, the applied electric field will mainly result in an axial deformation, ε_y^a, where the superscript 'a' represents actuator. Consider the fact that the bonding layer is much thinner than the actuator, the axial stress and deformation are assumed to be uniform across the thickness of the bonding layer as well. The interfacial shear stress between different layers is denoted as τ, as shown in Figure 4.2. u^+ and u^- in Figure 4.2 represent the displacements on the upper and lower surface of the bonding layer, respectively.

4.1.1 The Bonding Layer

Equation (3.3) can also be used to model the bonding layer between the actuator and the host structure. Similar steps are followed, and the resulting equation for the bonding layer is as follow:

$$-\tau = (\frac{\mu_b}{h'} - \frac{i\omega c_b}{h'})(u^+ - u^-). \tag{4.3}$$

According to the continuity of the displacements, u^+ and u^- also represent the longitudinal displacements of the lower surface of the actuator and the upper surface of the host medium, respectively. Their expression can be obtained by analyzing the dynamic behaviours of the actuator and the host medium.

4.1.2 Modelling of the Actuator

The current study will focus on the case when the system is subjected to a high frequency electric field, which results in a wave propagation with the typical wave length comparable to the length of the actuator. Therefore, the inertia effect of the actuator must be considered. Similar to the sensor model

in Chapter 3, the equation of motion of the actuator can be expressed as

$$\frac{d\sigma_y^a}{dy} + \tau(y)/h + \rho_a \omega^2 u_y^a = 0 \tag{4.4}$$

where the superscript 'a' represents the actuator; σ_y^a, ρ_a, and u_y^a are the axial stress, the mass density, and the axial displacement of the actuator, respectively.

Two electrodes are used at the upper and the lower surfaces for the application of an electric field to the actuator. When a voltage $\Delta V = V^+ - V^-$ is applied across the two electrodes, a constant electric field $E_z = -\Delta V/h$ is generated. In this case,

$$\frac{\partial E_z}{\partial y} = 0. \tag{4.5}$$

By employing Equation (3.11), the axial stress of the actuator can be expressed as a function of the axial displacement u_y^a and the electric field E_z as

$$\sigma_y^a = E_a \frac{\partial u_y^a}{\partial y} - e_a E_z \tag{4.6}$$

where E_a and e_a are effective material constants defined in Equation (3.16). Substituting Equation (4.6) into Equation (4.4), Equation (4.4) becomes:

$$E_a \frac{\partial^2 u_y^a}{\partial y^2} + \rho_a \omega^2 u_y^a + p(y) = 0 \tag{4.7}$$

where $p(y) = \tau(y)/h$.

The two ends of the actuator can be assumed to be traction free. Therefore

the following boundary condition is applied:

$$\sigma_y^a = 0, \quad |y| = a. \tag{4.8}$$

Making use of the wave number and wave speed of the actuator defined by

$$k_a = \frac{\omega}{c_a}, \quad c_a = \sqrt{E_a/\rho_a}, \tag{4.9}$$

the longitudinal displacement of the actuator can be determined in terms of the shear stress τ as:

$$\begin{aligned} u_y^a(y) = f_E(y) - & \frac{\cos[k_a(a+y)]}{k_a E_a \sin 2k_a a} \int_{-a}^{a} \cos[k_a(\xi - a)] p(\xi) d\xi \\ & - \frac{1}{k_a E_a} \int_{-a}^{y} \sin[k_a(y-\xi)] p(\xi) d\xi \quad |y| < a \end{aligned} \tag{4.10}$$

where

$$f_E(y) = \varepsilon_0 \frac{\sin k_a y}{k_a \cos k_a a} \tag{4.11}$$

is the axial displacement due to the applied electric field, with

$$\varepsilon_0 = \frac{e_a E_z}{E_a}. \tag{4.12}$$

4.1.3 Dynamic Behaviour of the Host Medium

Since there is no additional mechanical load applied to the host medium, the stress field generated inside the host structure is only due to the existence of the shear stress caused by the actuator at the top of its surface. Therefore,

the following boundary conditions exist

$$\begin{cases} \sigma_{yz}(y,0) = -\tau & |y| < a, \\ \sigma_{yz}(y,0) = 0 & |y| > a, \end{cases} \quad , \quad \sigma_z(y,0) = 0 \tag{4.13}$$

Making use of the general solution for the elastic half plane give by Chapter 3, Equation (3.37) and (3.38), the dynamic displacement along the interface between the bonding layer and the host medium can be determined as

$$u_y^h(y,0) = \frac{1}{\pi\mu_h}\int_0^\infty \left(\frac{\beta k^2}{(2s^2-k^2)^2-4s^2\alpha\beta} + \frac{\lambda_0}{2s}\right)\int_{-a}^{a}\tau(\xi)\cos[s(y-\xi)]d\xi ds + \frac{\lambda_0}{2\pi\mu_h}\int_{-a}^{y}\int_{-a}^{a}\tau(\xi)\frac{1}{y-\xi}d\xi dy, \quad |y| < a \tag{4.14}$$

where the superscript and subscript 'h' represent the host medium, μ_h is the shear modulus of the matrix, and $\lambda_0 = 2(1-\nu_h)$ with ν_h being the Poisson's ratio.

4.1.4 Dynamic Load Transfer

By substituting Equation (4.10) and Equation (4.14) into Equation (4.3), Equation (4.3) can be rewritten as

$$-\frac{\cos[k_a(a+y)]}{k_a E_a \sin 2k_a a}\int_{-a}^{a}\cos[k_a(\xi-a)]p(\xi)d\xi - \frac{1}{k_a E_a}\int_{-a}^{y}\sin[k_a(y-\xi)]p(\xi)d\xi - \frac{1}{\pi\mu_h}\int_0^\infty\left[\frac{\beta k^2}{(2s^2-k^2)^2-4s^2\alpha\beta} + \frac{\lambda_0}{2s}\right]\int_{-a}^{a}\tau(\xi)\cos[s(y-\xi)]d\xi ds - \frac{\lambda_0}{2\pi\mu_h}\int_{-a}^{y}\int_{-a}^{a}\tau(\xi)\frac{1}{y-\xi}d\xi dy + \frac{h'}{\mu_b - i\omega c_b}\tau(y) = -f_E(y), \quad |y| < a \tag{4.15}$$

The general solution of Equation (4.15) can be expressed in terms of Cheby-

shev polynomials,

$$\tau(y) = \sum_{j=0}^{\infty} c_j T_j(y/a)/\sqrt{1-y^2/a^2} \tag{4.16}$$

where

$$T_j(y/a) = \cos(j\theta), \quad \cos\theta = y/a \tag{4.17}$$

If τ is expanded into N terms, and Equation (4.15) is satisfied at the following locations along the actuator

$$y = a\cos[\frac{l}{N+1}\pi], \quad l = 1, 2, \cdots, N, \quad |y| < a \tag{4.18}$$

Equation (4.15) becomes N linear algebraic equations in term of $\{c\} = \{c_0, c_1, \cdots, c_{N-1}\}^T$, the coefficients of Chebyshev expansion. These N equations can be written in the form of:

$$[Q^a]\{c\} = \{F^a\} \tag{4.19}$$

where $[Q^a]$ is the resulting known matrix, and $\{F^a\}$ is the applied load matrix, which are given as follow:

$$\begin{aligned} Q^a_{lj} = & \frac{\overline{h'}}{(\mu_b - i\omega c_b)} \cdot \frac{T_j(\eta^l)}{\sqrt{1-\eta^{l2}}} - \pi \frac{\cos[\overline{k}_a(1+\eta^l)]}{\overline{k}_a E_a \overline{h}\sin(2\overline{k}_a)} P_j^2 \\ & + \frac{1}{\overline{k}_a E_a \overline{h}} \int_{\cos^{-1}\eta^l}^{\pi} \sin([\overline{k}_a(\cos\theta - \eta^l)]\cos(j\theta)d\theta \\ & - \frac{1}{\mu_h}\int_0^{\infty} P_j^1 \left(\frac{\overline{\beta}\overline{k}^2}{[(2\overline{s}^2 - \overline{k}^2)^2 - 4\overline{s}^2\overline{\alpha}\overline{\beta}]} + \frac{\lambda_0}{2\overline{s}}\right) d\overline{s} + \frac{\lambda_0}{2\mu_h} P_j^3 \end{aligned} \tag{4.20}$$

and

$$\{F^a\} = \frac{f_E(\eta^l)}{a} = \varepsilon_0 \frac{\sin \overline{k}_a \eta^l}{\overline{k}_a \cos \overline{k}_a} \tag{4.21}$$

where

$$\eta^l = y^l/a, \quad \overline{k} = ka, \quad \overline{k}_a = k_a a, \quad \overline{s} = sa. \tag{4.22}$$

The parameters P_j^1, P_j^2 and P_j^3 in Equation 4.20 are given by

$$\begin{aligned} P_j^1 &= J_j(\overline{s}) \begin{cases} (-1)^n \sin(\overline{s}\eta^l) & j = 2n+1 \\ (-1)^n \cos(\overline{s}\eta^l) & j = 2n \end{cases} \\ P_j^2 &= J_j(\overline{k}_a) \begin{cases} (-1)^n \sin(\overline{k}_a) & j = 2n+1 \\ (-1)^n \cos(\overline{k}_a) & j = 2n \end{cases} \\ P_j^3 &= \begin{cases} \frac{[\cos(j \cos^{-1} \eta^l) - (-1)^j]}{j} & j \neq 0 \\ 0 & j = 0 \end{cases} \end{aligned} \tag{4.23}$$

with J_j ($j = 1, 2 \cdots$) and T_j being the Bessel functions of the first kind and the Chebyshev polynomials, respectively. $\overline{\alpha}$, $\overline{\beta}$ can be directly obtained from α, β defined by Equation (3.39) in Chapter 3, with s and k being replaced by $\overline{s}$ and $\overline{k}$, respectively.

Compared with $[Q^s]$ obtained in Equation (3.58), $[Q^a]$ in Equation (4.20) doesn't change much. The only difference is the Young's Modulus of the actuator, E_a, is replaced by the material parameter $\overline{E}_s$. But the expression of $[F^a]$ in Equation (4.21) varies a lot from $[F^s]$ in Equation (3.59). $[F^a]$ is a result of the applied electric field; while $[F^s]$ is due to the induced incident wave.

By using Equation (4.19), the coefficients of Chebyshev Polynomials, $\{c\}$,

can be obtained. It can then be used to determine the interfacial shear stress τ between the actuator and the host structure, by using Equation (4.16).

4.2 Results and Discussion

This section will be devoted to the discussion about how the load transfer from the actuator to the host structure be affected by different parameters, such as the material properties of the bonding layer, the loading frequency, the material combination, actuator geometries, and so on. The material combination is represented by the material mismatch parameter q, whose definition is given by Equation (3.64). The length-to-thickness ratio of the actuator is denoted by v, which is defined by Equation (3.65).

The material constants of the piezoceramic (PZT) actuator are selected to be the same as those of the PZT sensor used in Chapter 3, as shown in Table 3.1. The material constants of the host medium and the bonding layer are shown in Table 4.1. The Young's modulus of the host medium has been selected to result in a material mismatch parameter $q = \dfrac{\pi E_h}{2(1-\nu_h^2)E_a} = 1.0$. The mass densities of the actuator and the host medium, ρ_a and ρ_h, are assumed to be $2700Kg/m^3$. The loading frequency ka is selected ranging from 1.0 to 16.0, with $ka = 1.0$ corresponding to $0.09MHz$. The geometry of the actuator and the bonding layer are as follow: $a = 1cm$, $h = 0.5mm$, and the range of h'/a is from 0 to 0.032. Based on the current selection of material constants, the actuator geometry parameter $v = a/h = 20.0$.

The normalized interfacial shear stress $\tau^* = \tau/\sigma_B$, with $\sigma_B = qe_aE_z$, is an important indictor of the actuation efficiency, and represents the load transfer between the actuator and the host medium. In our discussion, the normalized interfacial shear stress will be used to investigate how different material

Table 4.1: Material Properties of the Host Medium and the Bonding Layer-Actuator System

Host medium	
Young's Modulus E_h (Pa)	5.2715×10^{10}
Poisson's Ratio ν_h	0.3
Bonding Layer	
Shear Modulus μ_b (Pa)	1.0×10^9

parameters affect the load transfer from the actuator to host medium.

4.2.1 The Effect of the Thickness of the Bonding Layer

As indicated in Equation (4.3), the parameter μ_b/h' represents the stiffness of the bonding layer. In the following discussion, μ_b is set to be a constant value, and only the value of h' is changed to obtain different stiffness of the bonding layer.

To investigate the load transfer between the actuator and the host medium, a serial of thickness, $h' = 0$, 10, 40, 80, 160 and 320 μm, is selected. Three loading frequencies, $ka = 1.0$, 4.0, and 8.0, are chosen to study how the normalized interfacial shear stress varies with the increase of the thickness of the bonding layer, when the system is subjected to electric fields with different loading frequencies. The results corresponding to these three loading frequencies are shown in Figure 4.3, Figure 4.4, and Figure 4.5, respectively.

As shown in Figure 4.3, high stress concentration around the tip of the actuator is observed when the actuator is perfectly bonded. Comparing the six curves in this figure, we can clearly see that, as the h' value increases from 0 to $320\mu m$, the shear stress level along the actuator between the interval of $y/a = 0 \sim 0.9$ shows very limited changes, but the stress concentration around the tip of the actuator, where $y/a = 1.0$, decreases significantly.

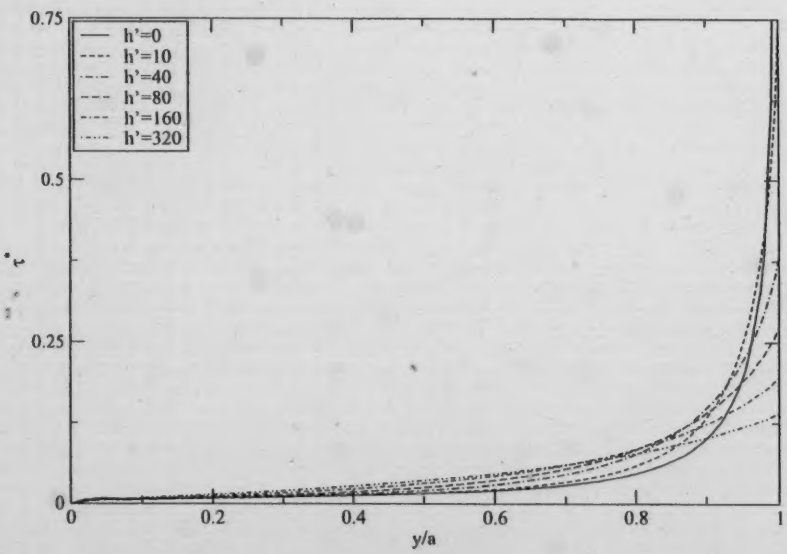

Figure 4.3: Normalized shear stress distribution along the actuator with different thicknesses of the bonding layer ($ka = 1.0$, $q = 1.0$, $v = 20.0$, $c_b = 10$)

Similar results are displayed in Figure 4.4 and Figure 4.5 for higher frequencies. But in these cases, with the increase of h' value, dramatic change in shear stress distribution along the actuator is observed. In Figure 4.4, when h' value is between 0 and $160\mu m$, the shear stress increases approaching the tip of the actuator. However, when $h' = 320\mu m$, the shear stress value decreases in the interval of $y/a = 0.6 \sim 1.0$. Similar phenomenon is observed in Figure 4.5. When h' value goes up to 160 and 320 μm, the stress value decreases as y/a increases from 0.8 to 1.0. In addition, with the increase of the thickness of the layer, the shear stress concentration near the tip of the actuator becomes less important. The results indicate that, with the increase of loading frequency, the effect of the thickness of the bonding layer on the load transfer between the actuator and the host medium becomes more and more significant.

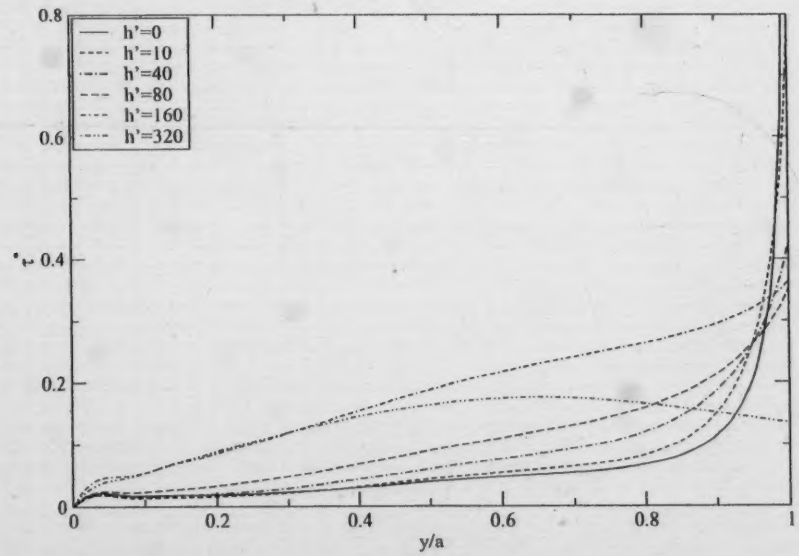

Figure 4.4: Normalized shear stress distribution along the actuator with different thicknesses of the bonding layer (ka=4.0, $q = 1.0$, $v = 20.0$, $c_b = 10$)

4.2.2 The Effect of the Coefficient of Viscosity

The coefficient of viscosity of the bonding layer also affects the load transfer between the actuator and the host medium, even though its effect may not be as significant as that of the thickness or the modulus of the layer. For the case where $ka = 5.0$ (corresponding to $0.45MHz$) and $h' = 100\mu m$, a serial of coefficients of viscosity of the bonding layer, c_b=10, 100, 1000, 3000, 10000 and 100000 $Pa \cdot s$, is selected, and the distribution of the normalized shear stress along the actuator with different selections of the coefficient of viscosity is shown in Figure 4.6.

Since in this case the thickness of the layer is quite significant, the shear stress concentration near the tip of the actuator is not obvious for low coefficient of viscosity ($c_b = 10 \sim 100\ Pa \cdot s$). As c_b continues to increase, high

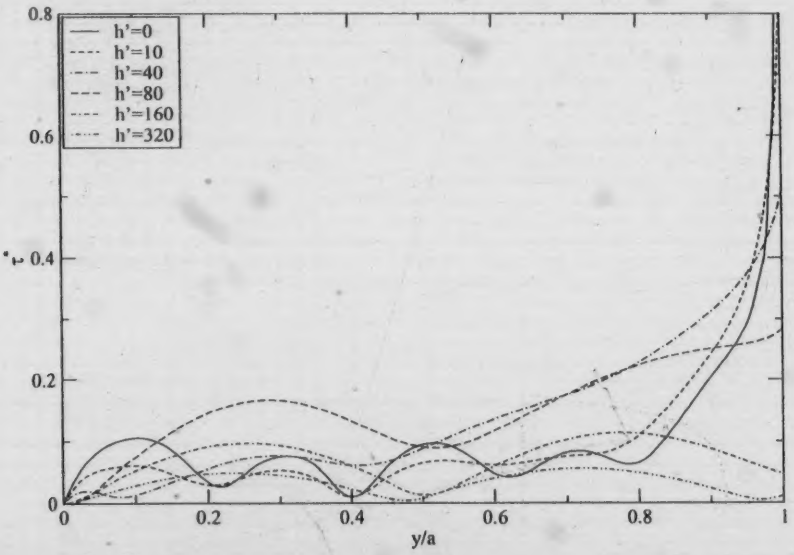

Figure 4.5: Normalized shear stress distribution along the actuator with different thicknesses of the bonding layer (ka=8.0, $q = 1.0$, $v = 20.0$, $c_b = 10$)

concentration of the shear stress around the tip of the actuator is observed. For high c_b value ($c_b = 100000\ Pa \cdot s$), the stress concentration around the tips becomes very significant. In fact, the stiffness of the bonding layer is increased with increasing c_b. When c_b is very high, the property of the layer is close to that under the perfect bonding condition.

4.2.3 The Effect of the Loading Frequency

The significant effect of the loading frequency upon the shear stress distribution has been observed by comparing the results shown in Figure 4.3, Figure 4.4 and Figure 4.5. To have a closer look, a serial of loading frequency values, $ka = 1.0$, 2.0, 4.0, 8.0 and 16.0, is selected, and two bonding conditions, $h' = 0$ and $h' = 100\mu m$, are considered.

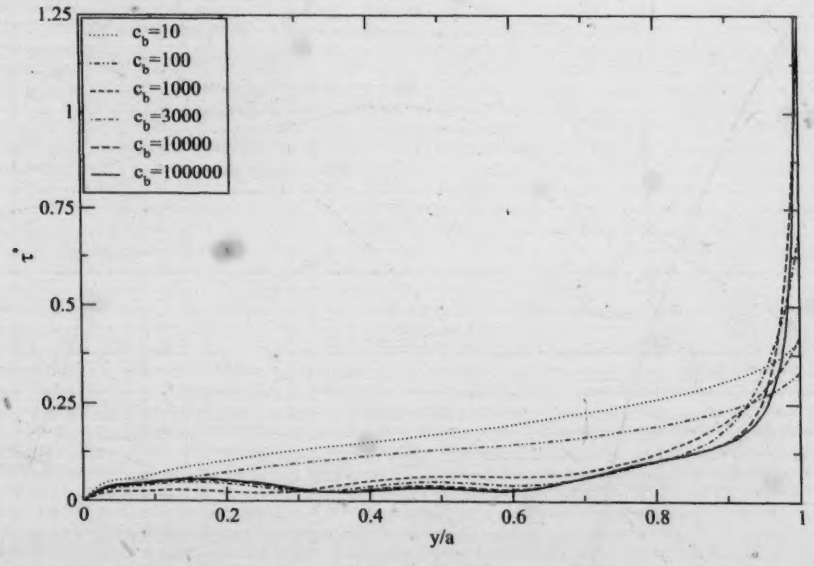

Figure 4.6: Normalized shear stress distribution with different coefficients of viscosity ($ka = 5.0$, $h' = 100$, $q = 1.0$, $v = 20.0$)

The normalized shear stress distribution for perfectly bonded actuator is depicted in Figure 4.7 for different loading frequencies. The results for the corresponding cases with a bonding layer ($h' = 100\mu m$) is given in Figure 4.8.

In Figure 4.7, the increase of the loading frequency results in an increase of the shear stress away from the tip of the actuator. Similar phenomenon is observed in Figure 4.8 where a bonding layer is included. However, with the increase of the loading frequency, the singular behaviour of the shear stress at the tip of the actuator becomes less obvious.

4.2.4 The Effect of the Material Mismatch

The material mismatch parameter $q = \dfrac{\pi E_h}{2(1-\nu_h^2)E_a}$ is an indicator of the relative modulus of the actuator to the host medium. For the current selection

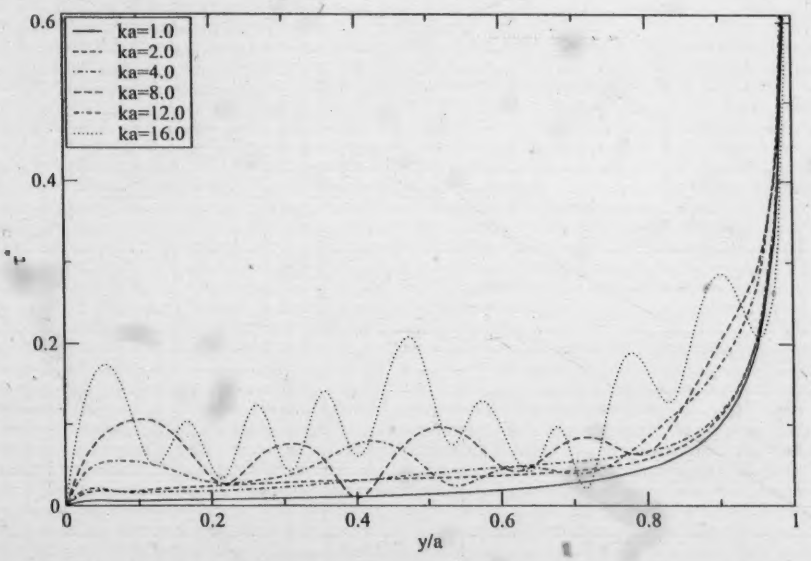

Figure 4.7: Normalized shear stress distribution with different loading frequencies ($h' = 0$, $q = 1.0$, $v = 20.0$)

of actuator, the bonding layer and host medium given in Table 3.1 and 4.1, $q = 1.0$. To study the effect of material mismatch q, the material constants of the actuator are fixed, and the shear modulus of the host medium is changed to achieve different material combinations. In this section, $q = 0.1$, 0.5, 1.0, 2.0 and 5.0 are chosen, and two bonding conditions, $h' = 0$ and $h' = 100\mu m$, are considered to investigate the effect of material combinations on the load transfer between the actuator and the host structure. The loading frequency is selected as $ka = 5.0$, and the normalized shear stress distribution curves under these two bonding conditions are shown in Figure 4.9 and Figure 4.10, respectively.

In Figure 4.9, with the decrease of q, an increase of the shear stress level can be observed. When q approaches 0.1, corresponding to a stiff actuator,

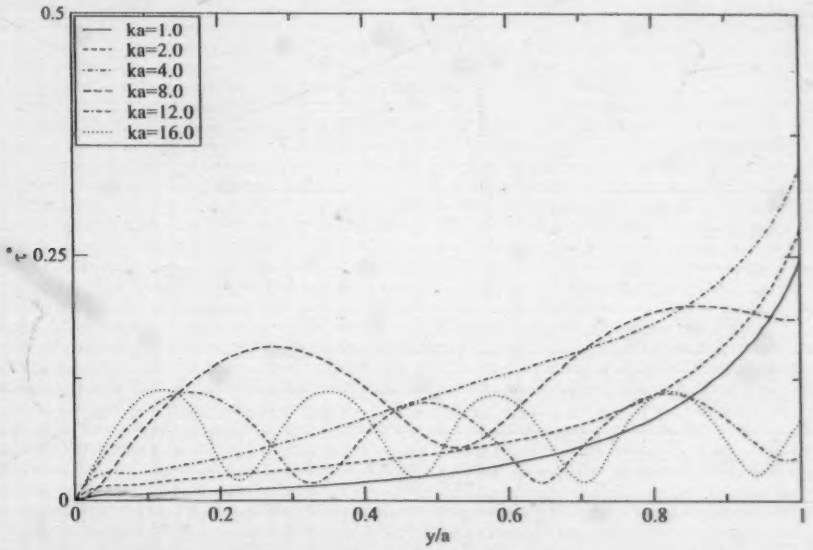

Figure 4.8: Normalized shear stress distribution with different loading frequencies ($h' = 100$, $q = 1.0$, $v = 20.0$, $c_b = 10$)

significant increase in the shear stress along the actuator is observed.

Figure 4.10 shows very similar results, which is for the case where the bonding layer is included. In this case, the singular behaviour of the shear stress at the tip of the actuator is significantly reduced. This indicates that the material mismatch affects the shear stress distribution more when the bonding condition is not perfect, at lease for the currently used bonding layer. Proper selection of material combination, if possible, will increase the actuation efficiency of the actuator.

4.2.5 The Effect of the Geometry of the Actuator

The effect of the geometry of actuator upon the load transfer between the actuator and the host medium is also studied. The actuator geometry is rep-

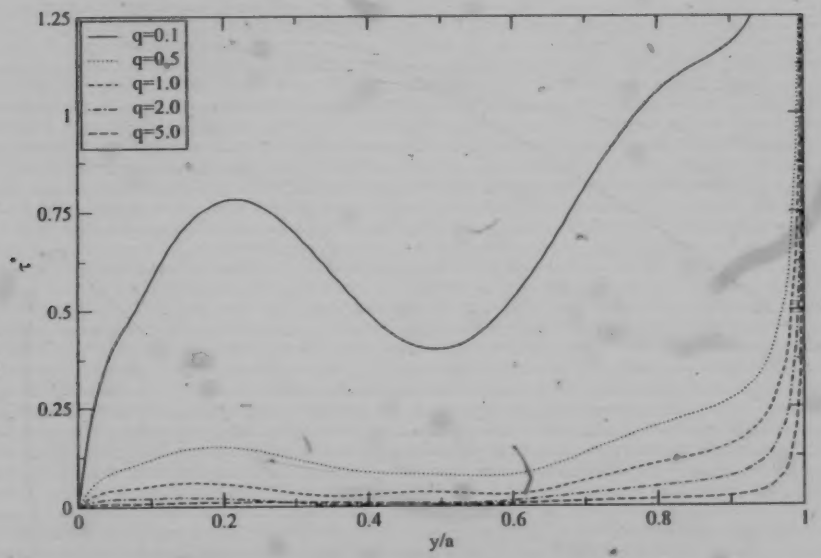

Figure 4.9: Normalized shear stress distribution along the actuator with different material combinations ($ka = 5.0$, $h' = 0$, $v = 20.0$)

resented by the ratio of its length to its height, $v = a/h$. Four v values, v=5.0, 10.0, 15.0 and 20.0, are selected to evaluate its effect. $ka = 5.0$ is chosen as the loading frequency, and two bonding conditions, $h' = 0$ and $h' = 100\ \mu m$ are considered. The results with $h' = 0$ and $h' = 100\mu m$ are displayed in Figure 4.11 and Figure 4.12, respectively.

As shown in Figure 4.11, the decrease in the v value makes shear stress distribution less concentrated around the tips of the actuator. Increase of shear stress level along the actuator due to decreasing v value is also observed.

When a bonding layer is included, as shown in Figure 4.12, the stress concentration around the tip of the actuator is dramatically reduced in comparison with its corresponding curve in Figure 4.11. It is also observed that the shear stress distribution along the actuator has also been significantly affected in

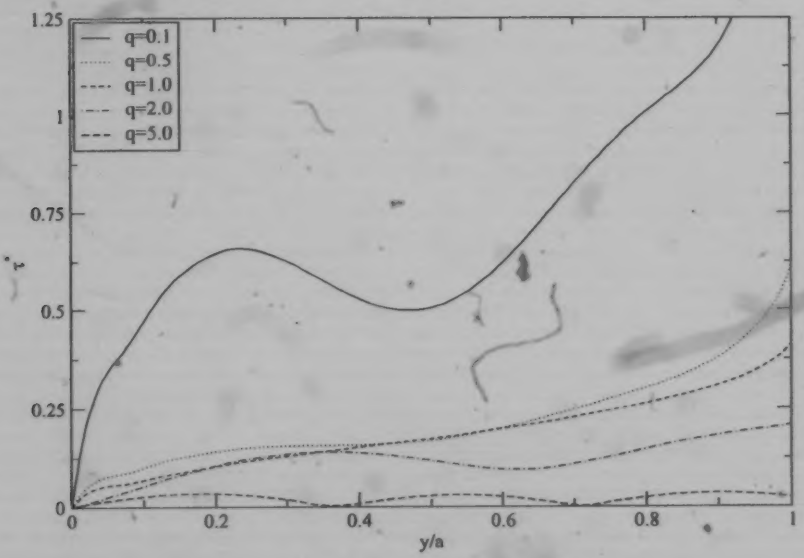

Figure 4.10: Normalized shear stress distribution along the actuator with different material combinations ($ka = 5.0$, $h' = 100$, $v = 20.0$, $c_b = 10$)

comparison with the result given by Figure 4.11.

4.3 Concluding Remarks

This chapter studies the effect of different material parameters of the bonding layer and of the actuator on the load transfer from the actuator to the host medium, when a high frequency electric field is applied to the actuator. The high frequency electric field considered in this Chapter starts from $ka = 1.0$. Analytical method is provided, and numerical simulation is conducted for special cases. The following conclusions are obtained:

(1) For relatively low frequency cases, $ka = 1.0$ and 4.0, the increase of the bonding layer thickness, from 0 to $320\mu m$ will increase the shear stress distribution level along the internal of the actuator, by up to 50%

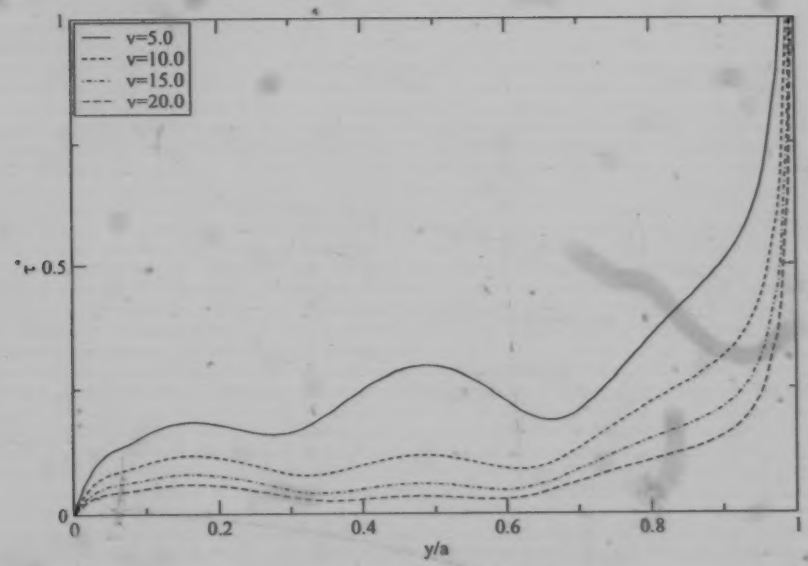

Figure 4.11: Normalized shear stress distribution with different actuator geometries ($ka = 5.0, h' = 0$, $q = 1.0$)

($ka = 1.0$) and by up to 97% ($ka = 4.0$) at $y/a = 0.9$, where strain concentration begins to occur, and decrease the strain concentration at the tips of the actuator. For relatively high frequency cases, $ka > 4.0$, the increase of the bonding layer thickness results in a shear stress distribution curve along the actuator varying significantly from that obtained by perfectly bonded actuator, both in shape and amplitude. The changes in amplitude may be as high as 600% (obtained when $h' = 40\mu m$ at $y/a = 0.4$), comparing to the result obtained at the same location but under perfect bonding condition.

(2) Based on the current simulation, for using the currently selected actuator to induce elastic wave into the host structure, the loading frequency of the electric field $ka <= 5.0$ is appropriate to select.

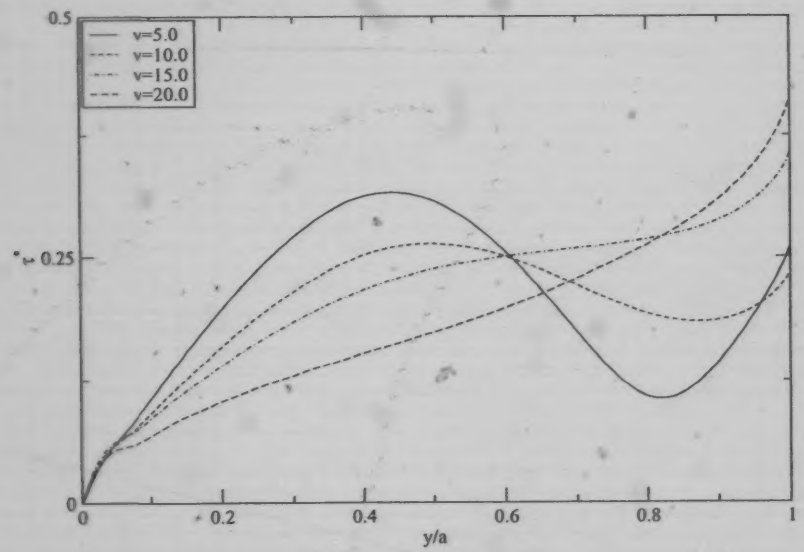

Figure 4.12: Normalized shear stress distribution with different actuator geometries ($ka = 5.0, h' = 100$, $q = 1.0$, $c_b = 10$)

(3) The material combination and actuator geometry show more influence on the shear stress distribution when the bonding condition is not perfect. Based on the current material selection, the preferred range for the material mismatch parameter q is from 0.5 to 2.0, and that for the actuator geometry parameter v is from 15.0 to 20.0, when the loading frequency $ka <= 5.0$, and the thickness of the bonding layer $h' <= 100\mu m$. Otherwise, if q is beyond this range, or v is smaller than 15.0, considerable difference can be observed between the shear stress distributions along the actuator when the bonding layer is included and when perfect bonding condition is assumed.

Chapter 5

Conclusions and Future Work

5.1 Contributions and Conclusions

The focus of this thesis is on the effect of the bonding layer on the dynamic electromechanical behaviour of piezoelectric sensors and actuators. The contributions of this work can be summarized as:

(1) A one dimensional sensor/actuator dynamic model with a bonding layer, which undergoes a shear deformation, is proposed. Based on this model, numerical simulations are conducted under different geometric and loading conditions to study the effects of the bonding layer properties on the dynamic load transfer between the sensors/acutators and the host structures.

(2) The simulation results indicate that, for relatively low frequency cases, with the increase of the bonding layer stiffness, the amplitude of the strain distribution along the sensor or the shear stress distribution along the actuator gets higher, which corresponds to an increase in sensor/actuator efficiency. For relatively high frequency cases, however, the strain distribution along the sensor or the shear stress distribution along the actu-

ator becomes very complicated and unpredictable with the decrease of the bonding layer stiffness.

(3) With the existence of the bonding layer, the stress concentration at the tips of the sensor/actuator becomes more and more obvious with the increase of the bonding layer stiffness, which will make the sensor/actuator more likely to peel off from the host structure. Therefore, there is a trade-off in selecting the optimal adhesive, i.e. the stiffness of the adhesive should be increased to improve the sensor/actuator efficiency, but high stiffness of the adhesive should also be avoided in order to prevent sensors/actuators from pealing off from the host structure.

(4) The results of the strain distribution along the sensor and the shear stress distribution along the actuator obtained when a bonding layer is included are compared with the prediction by perfectly bonded sensors/actuators, when other conditions, such as loading frequency, and material selection are the same. Significant difference between these two types of results in the dynamic response of the sensor/actuator system is observed. It should be mentioned that, only if the layer thickness becomes very small, the current model could provide similar phenomena to that by perfectly bonded sensors/actuators. But in these cases, the bonding layer becomes so thin that it is too difficult to achieve in reality. Therefore, in general cases, the bonding condition can not be simply assumed to be perfect.

Based on the analysis conducted in Chapter 3 and Chapter 4, the following specific conclusions, which are potentially useful in the design of piezoelectric sensors/actuators for SHM systems, can be obtained:

(1) High stiffness of the bonding layer is preferred. This corresponds to thin bonding layer, high layer modulus, or high viscosity. According to the current simulation, $h' <= 100\mu m$ is a good choice for both the sensor and actuator system. Even though this h' value range is relatively hard to achieve in real experiment condition, the purpose of increasing the bonding layer stiffness can also be achieved by increasing the modulus or the viscosity of the bonding layer. However, since the strain concentration around the tips of the sensor/actuator increases as the bonding layer gets stiffer, attention should also be paid to make sure the sensor/actuator will not peel off from the host medium.

(2) As the loading frequency increases, the disturbance of the sensor on the strain field to be measured becomes more and more significant. When using piezoelectric patches to detect high frequency signals, the loading frequency should not be too high in order to ensure accuracy. Based on the current material selection, $ka <= 2.0$ and $ka <= 5.0$ are more appropriate for the sensor system and the actuator system, respectively.

(3) The material combination of the sensor/actuator and the host structure needs to be carefully selected. Based on the current simulation, the material mismatch parameter q between 0.5 and 2.0 is acceptable. If q is beyond this range, it will increase the effects of the bonding layer on the load transfer between the sensor/actuator and the host structure. In other words, significant difference of the load transfer can be observed between the case when the bonding layer is included and the one when perfect bonding condition is assumed.

(4) Thin sheet sensor is preferred. Based on the current simulation, a length-

to-thickness ratio $q >= 15.0$ is acceptable. If q value is smaller than 15.0, the sensor will predict a strain significantly different from that generated by the incident field, which is supposed to be measured. However, for the currently selected sensor, whose length is fixed to be $1cm$, $q > 20.0$ is not very easy to achieve. Therefore, q between 15.0 and 20.0 is appropriate.

5.2 Future Work

The objective of this thesis is to study the effect of the bonding layer properties on the dynamic electromechanical behaviour of a sensor/actuator system. The simulation part is done in this thesis, and future studies in the following areas are suggested:

(1) Corresponding experimental work needs to be conducted to verify the simulation results obtained by using the current sensor/actuator model. Proper modification of the sensor/actuator model may be needed according to experiment results.

(2) In the next step, cracks with different sizes and orientations may be introduced into the host medium. The wave reflected by the cracks may be collected by piezoelectric sensors and identification of cracks may be conducted, both theoretically and experimentally.

(3) The current two dimensional model can be further extended into a 3-D model in order to provide more accurate simulation results for the real sensor/actuator system, which, in reality, is always three dimensional.

(4) Besides, simulation and experiments need to be conducted for different selections of existing adhesives, sensor/actuator and host medium mate-

rials in order to give more concrete suggestions about the optimal design of sensor/actuator systems.

BIBLIOGRAPHY

[1] C. Boller, 2000, Next generation structural health monitoring and its integration into aircraft design, International Journal of Systems Science, 31: 1333-1349.

[2] G. Park, C. R. Farrar, F. L. di Scalea, S. Coccia, 2006, Performance assessment and validation of piezoelectric active-sensors in structural health monitoring, Smart Materials and Structures, 15: 1673-1683.

[3] C. P. Providakis, D-P N. Kontoni, M. E. Voutetaki, 2007, Development of an electromechanical admittance approach for application in the vibration control of intelligent structures, Smart Materials and Structures, 16: 275-281.

[4] M. Yang, P. Qiao, 2005, Modeling and experimental detection of damage in various materials using the pulse-echo method and piezoelectric sensors/actuators, Smart Mmaterials and Structures, 14(6): 1083-1100.

[5] M. W. Lin, C. A. Rogers, 1993a, Modeling of the actuation mechanism in a beam structure with induced strain actuators, Proceeding of AIAA/ASCE/ASME/ASC 34th Structures, Structural Dynamics and Materials Conference, AIAA Inc., Washington, DC, Part VI, 3608-3617, La-Jolla, CA, 19-22, April.

[6] M. W. Lin, C. A. Rogers, 1993b, Actuation response of a beam structure with induced strain actuators, Adaptive Structures and Material Systems, AD 35: 129-139.

[7] V. V. Varadan, J. Kim, V. K. Varadan, 1997, Modeling of piezoelectric sensor fidelity, IEEE Transactions on Ultrasonics, Ferroelectrics, and Frequency Control, 44(3): 538-547.

[8] J. Sirohi, I. Chopra, 2000, Fundamental understanding of piezoelectric strain sensors, Journal of Intelligent Material Systems and Structures, 11(4): 246-257.

[9] F. L. di Scalea, H. Matt, I. Bartoli, 2007, The response of rectangular piezoelectric sensors to Rayleigh and Lamb ultrasonic waves, The Journal of the Acoustical Society of America, 121(1): 175-187.

[10] W. G. Cady, 1922, The piezoelectric resonator, Proceedings of I. R. E., 10: 83-114.

[11] G. W. Pierce, 1925, Piezoelectric crystal oscillators applied to the precision measurement of the velocity of sound in air and CO_2 at high frequencies, Proceedings of the American Academy of Arts and Sciences, 60: 269-302.

[12] W. P. Mason, 1934, Electrical wave filters employing quartz crystals as elements, Bell System Technical Journal, XIII, 450-452.

[13] J. F. Tressler, S. ALkoy, R. E. Newnham, 1998, Piezoelectric sensors and sensor materials, Journal of Electroceramics, 2(4): 257-272.

[14] D. Berlincourt, 1992, Piezoelectric ceramic compositional development, The Journal of the Acoustical Society of America, 91(5): 3034-3040.

[15] B. Jaffe, W. R. Cook, J. Jaffe, 1971, Piezoelectric ceramics, Academic Press, New York, p.148.

[16] T. Ikeda, 1990, Fundamentals of piezoelectricity, Oxford University Press, New York, NY, p.209.

[17] R. C. Pohanka, P. L. Smith, 1988, Electronic ceramics, properties, devices and applications, (edited by L. N. Levinson), Chapter 2, Marcel Dekker, New York.

[18] H. T. Banks, P. R. Emeric, 1998, Detection of non-symmetrical damage in smart plate-like structures, Journal of Intelligent Material Systems and Structures, 9(10): 818-828.

[19] SHD. Valdes, C. Soutis, 1999, Application of the rapid frequency sweep technique for delamination detection in composite laminates, Advanced Composites Letters, 8(1): 19-23.

[20] A. Chattopadhyay, C. Nam, Y. Kim, 2000, Damage detection and vibration control of a delaminated smart composite plate, Advanced Composites Letters, 9(1): 7-15.

[21] H. A. Winston, F. Sun, B. S. Annigeri, 2001, Structural health monitoring with piezoelectric active sensors, Journal of Engineering for Gas Turbines and Power, 123(2): 353-358.

[22] V. Giurgiutiu, A. N. Zagrai, 2002, Embedded self-sensing piezoelectric active sensors for on-line structural identification, Journal of Vibration and Acoustics, 124(1): 116-125.

[23] S. C. Gales, W.K. Chiu, J. J. Paul, 1993, Use of piezoelectric films in detecting and monitoring damage in composites, Journal of Intelligent-Material Systems and Structures, 4: 330-336.

[24] A. Kugi, K. Schlacher, H. Irschik, 1999, Infinite-dimensional control of nonlinear beam vibrations by piezoelectric actuator and sensor layers, Nonlinear Dynamics, 19(1): 71-91.

[25] J. M. Sloss, J. C. Brucha, I. S. Sadekc, S. Adalid, 2003, Piezo patch sensor/actuator control of the vibrations of a cantilever under axial load, Composite Structures, 64(3-4): 423-428.

[26] Y-S Lee, S. J. Elliott, P. Gardonio, 2003, Matched piezoelectric double sensor/actuator pairs for beam motion control, Smart Materials and Structures, 12(4): 541-548.

[27] J. Pan, 1994, Further studies of the dynamic response of a simply supported beam excited by a pair of out-of-phase piezoelectric actuators, Journal of Intelligent Material Systems and Structures, 5: 654-664.

[28] I. Y. Shen, 1995, Bending and torsional vibration control of composite beams through intelligent constrained-layer damping treatments, Smart Materials and Structures, 4: 340-355.

[29] Q. Wang, S. T. Quek, 2000, Flexural vibration analysis of sandwich beam coupled with piezoelectric actuator, Smart Materials and Structures, 9(1): 103-109.

[30] H. T. Banks, K. Ito, Y. Wang, 1993, Computational methods for identifications and feedback control in structures with piezoceramic actuators and sensors, Journal of Intelligent Material Systems and Structures, 4: 469-476.

[31] B. G. Fitzpatrick, 1997, Shape matching with smart material structures using piezoceramic actuators, Journal of Intelligent Material Systems and Structures, 8: 876-882.

[32] C. M. Wang, K. K. Ang, A. Ajit, 1999, Shape control of laminated cantilevered beams with piezoelectric actuators, Journal of Intelligent Material Systems and Structures, 10(2): 164-175.

[33] D. B. Koconis, L. P. Kollar, G. S. Springer, 1994, Shape control of composite plates and shells with embedded actuators I. Voltages specified, Journal of Composite Material, 28(4): 415-458.

[34] D. B. Koconis, L. P. Kollar, G. S. Springer, 1994, Shape control of composite plates and shells with embedded actuators, II. Desired shape specified, Journal of Composite Materials, 28(3): 262-285.

[35] K. Chandrashekhara, S. Varadarajan, 1997, Adaptive shape control of composite beams with piezoelectric actuators, Journal of Intelligent Material Systems and Structures, 8(2): 112-124.

[36] H. Irschik, C. Adam, R. Heuer, F. Ziegler, 1997, An exact solution for static shape control using piezoelectric actuation, Solid Mechanics and its Applications, 60: 247-258.

[37] A. Achuthan, A. K. Keng, W. C. Ming, 2001, Shape control of coupled nonlinear piezoelectric beams, Smart Materials and Structures, 10(5): 914-924.

[38] C. Liang, F. P. Sun, C. A. Rogers, 1994, Coupled electro-mechanical analysis of adaptive material system-determination of the actuator power consumption and energy transfer, Journal of Intelligent Material Systems and Structures, 5: 12-20.

[39] F. P. Sun, Z. Chaudhry, C. A. Rogers, M. Majmundar, C. Liang, 1995, Automated real-time structure health monitoring via signature pattern recognition, Proceedings of the SPIE Conference on Smart Structures and Materials, San Diego, California, 2443: 236-247.

[40] J. W. Ayres, F. Lalande, Z. Chaudhry, C. A. Rogers, 1998, Qualitative impedance-based health monitoring of civil infrastructures, Smart Materials and Structures, 7(5): 599-605.

[41] G. Park, H. H. Cudney, D. J. Inman, 2000, Impedance-based health monitoring of civil structural components, ASCE Journal of Infrastructure Systems, 2000, 6: 153-160.

[42] G. Park, H. H. Cudney, D. J. Inman, 2001, Feasibility of using impedance-based damage assessment for pipeline structures, Earthquake Engineering and Structural Dynamics, 30: 1463-1474.

[43] E. Monaco, F. Franco, L. Lecce, 2000, Experimental and numerical activities on damage detection using magnetostrictive actuators and statistical analysis, Journal of Intelligent Material Systems and Structures, 11(7): 567-578.

[44] C. K. Soh, K. K-H. Tseng, S. Bhalla, A. Gupta, 2000, Performance of smart piezoceramic patches in health monitoring of a RC bridge, Smart Materials and Structures, 9(4): 533-542.

[45] V. Jr. Lopes, G. Park, H. H. Cudney, D. J. Inman, 1999, Smart structures health monitoring using artificial neural network; 2nd International Workshop of Structural Health Monitoring, Stanford University, 976-985.

[46] F. K. Chang, 1995, Built-in damage diagnostics for composite structures, Proceedings of the 10th International Conference on Composite Structures (ICCM-10), 5: 283-289.

[47] X. Lin, F. G. Yuan, 2000, Pre-stack reverse time migration in structural health monitoring, 41st AIAA/ASME/ASCE/AHS/ASc Structures, Structural Dynamics and Materials Conference and Exhibit, Atlanta, 1984-1994.

[48] J. M. Park, J. W. Kong, D. S. Kim, D. J. Yoon, 2005, Nondestructive damage detection and interfacial evaluation of single-fibers/epoxy composites using PZT, PVDF and P(VDF-TrFE) copolymer sensors, Composites Science and Technology, 65(2): 241-256.

[49] C. R. Farrar, S. W. Doebling, D. A. Nix, 2001, Vibration-based structural damage identification, Philosophical Transactions: Mathematical, Physical and Engineering Sciences, 359: 131-149.

[50] C. Biemans, W. J. Staszewski, Ç. Boller, G. R. Tomlinson, 1999, Crack detection in metallic structures using piezoceramic sensors, Damage Assessment of Structures Key Engineering Materials, 167(1): 112-121.

[51] V. Giurgiutiu, J. J. Bao, W. Zhao, 2003, Piezoelectric wafer active sensor embedded ultrasonics in beams and plates, Experimental Mechanics, 43(4): 428-449.

[52] S. M. Prasad, K. Balasubramaniam, C. V. Krishnamurthy, 2004, Structural health monitoring of composite structures using Lamb wave tomography, Smart Materials and Structures, 13(5): N73-N79.

[53] X. Lin, F. G. Yuan, 2005, Experimental study applying a migration technique in structural health monitoring, Structural Health Monitoring, 4(4): 341-353.

[54] M. A. Moetakef, S. P. Joshi, K. L. Lawrence, 1996, Elastic wave generation by piezoceramic patches, AIAA Journal, 34(10): 2110-2117.

[55] G. P. Gibbs, C. R. Fuller, 1992, Excitation of thin beams using asymmetric piezoelectric actuators, The Journal of the Acoustical Society of America, 92: 3221-3227.

[56] M. Tracy, F. K. Chang, 1998, Identifying impacts in composite plates with piezoelectric strain sensors, Part I: theory, Journal of Intelligent Materials Systems and Structures, 9(11): 920-928.

[57] W. Lestari, P. Z. Qiao, 2005, Application of wave propagation analysis for damage identification in composite laminated beams, Journal of Composite Material, 39(22): 1967-1984.

[58] V. Giurgiutiu, A. Zagrai, J. J. Bao, 2002, Piezoelectric wafer embedded active sensors for aging aircraft structural health monitoring, Structural Health Monitoring, 1:41-61.

[59] M. J. Sundaresan, A. Ghoshal, M. J. Schulz, 2002, A continuous sensor for damage detection in bars, Smart Materials and Structures, 11(4): 475-488.

[60] D. N. Alleyne, P. Cawley, 1992, Optimization of Lamb wave inspection techniques, NDT and E International, 25(1): 11-22.

[61] J. Jin, S. T. Quek, Q. Wang, 2005, Wave boundary element to study Lamb wave propagation in plates, Journal of Sound and Vibration, 288: 195-213.

[62] B. L. Wang, Y. W. Mai, 2002, Fracture of a piezoelectric material layer bonded by two elastic layers, International Journal of Engineering Science 40(15): 1697-1727.

[63] B. Zhang, J. Zhang, 2005, Electromechanical interaction behaviors of piezoelectric sensor and actuator on elastic substrate, Journal of Intelligent Material Systems and Structures, 16(7-8): 589-595.

[64] E. F. Crawley, D. J. Luis, 1987, Use of piezoelectric actuators as elements of intelligent structures, AIAA Journal, 25(10): 1373-1385.

[65] E. F. Crawley, E. H. Anderson, 1990, Detailed models of piezoelectric actuation of beams, Journal of Intelligent Material Systems and Structures, 1: 4-25.

[66] S. Im, S. N. Atluri, 1989, Effects of a piezo-actuator on a finite deformation beam subjected to general loading, AIAA Journal, 27: 1801-1807.

[67] X. D. Wang, 1999, Coupled electromechanical behaviour of piezoelectric actuators in smart structures, Journal of Intelligent Material System and Structures, 10(3): 232-241.

[68] X. D. Wang, G. L. Huang, 2001, Wave propagation in electromechanical structures: induced by surface bonded piezoelectric actuators, Journal of Intelligent material System and Structures, 12(2): 105-115.

[69] X. D. Wang, G. L. Huang, 2006, Wave propagation generated by piezoelectric actuators attached to elastic substrates, Acta Mechanica, 183: 155-176.

[70] X. D. Wang, and G. L. Huang, 2006, The coupled dynamic behaviour of piezoelectric sensors bonded to elastic media, Journal of Intelligent Material Systems and Structures, 17: 883-894.

[71] P. Akella, X. Chen, W. Cheng, D. Hughes, J. T. Wen, 1994, Modelling and control of smart structures with bonded piezoelectric sensors and actuators, Smart Materials and Structures, 3: 344-353.

[72] B. C. Nakra, 2005, Vibration control in machines and structures using viscoelastic damping, Journal of Sound and Vibration, 211(3): 449-465.

[73] J. M. Park, D. S. Kim, S. B. Han, 2000, Properties of interfacial adhesion for vibration controllability of composite materials as smart structures, Composites Science and Technology, 60: 1953-1963.

[74] M. Pietrzakowski, 2001, Active damping of beams by piezoelectric system: effects of bonding layer properties, Solids and Structures, 38: 7885-7897.

[75] A. R. de Faria, 2003, The impact of finite stiffness bonding on the sensing effectiveness of piezoelectric patches, Smart Materials and Structures, 12: N5-N8.

[76] Y. E. Park, 1990, Crack extension force in a piezoelectric material, ASME Journal of Applied Mechanics, 57: 647–653.

[77] C. K. Lee, and F. C. Moon, 1989, Laminated piezopolymer plates for torsion and bending sensors and actuators, Journal of the Acoustic Society of America, 85(6): 2432-2439.

[78] Y. E. Park, 1990, Crack extension force in a piezoelectric material, ASME Journal of Applied Mechanics, 57: 647-653.

[79] J. D. Achenbach, 1973, Wave propagation in elastic solids, North-Holland Publishing Company, Amsterdam, New York, Oxford.

Appendix A: Plane Elastic Waves in Elastic Half-Spaces

The presence of a discontinuity in the material properties generally produces a significant influence on the systems of wave propagation through the medium [79]. In such a composite medium, the system of plane wave propagation can be considered as an incident wave, and it will be reflected and refracted at the interface between two different media.

A.1 Plane Harmonic Waves

A convenient expression of a plane harmonic displacement wave is given by

$$\vec{U} = A\vec{d}\,\exp[ik(\vec{x}\cdot\vec{p} - ct)] \qquad (1)$$

where $\vec{d}$ and $\vec{p}$ are unit vectors defining the directions of motion and propagation, respectively; $\vec{x}$ is the position vector, A denotes the amplitude of the wave, and k and c are wave-number and wave speed, respectively.

There are two types of plane harmonic waves:

- Longitudinal waves (P-wave) for which $\vec{d} = \pm\vec{p}$ and $c = c_L$
- Transverse waves (S-wave) for which $\vec{d}\cdot\vec{p} = 0$ and $c = c_T$

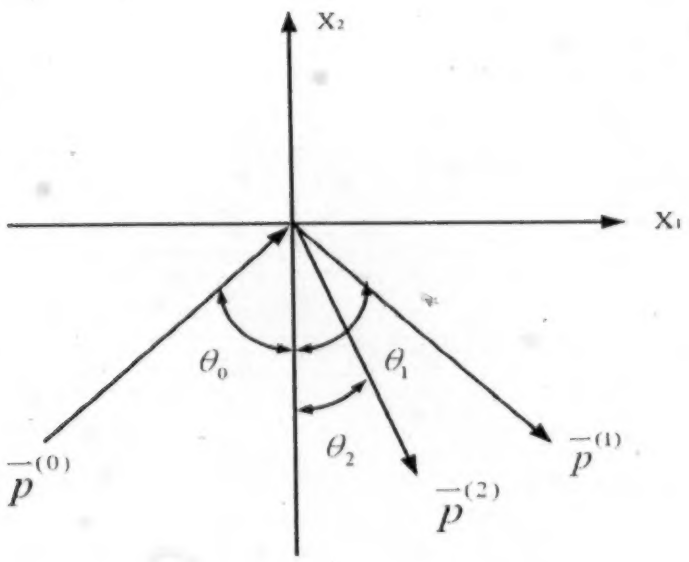

Figure 1: Reflection of a P-wave

where c_L and c_T represent the wave speed of longitudinal wave and transverse wave, respectively.

A.2 Reflection of P-Wave

By using the notation introduced in Equation 1, the incident P-wave as well as the reflected P-wave and S-wave can be denoted as

$$\overrightarrow{U}^{(n)} = A_n \overrightarrow{d}^{(n)} \exp[ik_n(x_1 p_1^{(n)} + x_2 p_2^{(n)} - c_n t)] \tag{2}$$

where the index n serves to label the various types of waves, as shown in Figure 1.

The index n is assigned the value $n = 0$ for the incident P-wave, and we

have

$$d_1^{(0)} = \sin\theta_0, \quad d_2^{(0)} = \cos\theta_0 \tag{3}$$

$$p_1^{(0)} = \sin\theta_0, \quad p_2^{(0)} = \cos\theta_0, \tag{4}$$

$$c_0 = c_L \tag{5}$$

The reflected P-wave is labelled by $n = 1$, and we have

$$d_1^{(1)} = \sin\theta_1, \quad d_2^{(1)} = -\cos\theta_1 \tag{6}$$

$$p_1^{(1)} = \sin\theta_1, \quad p_2^{(1)} = -\cos\theta_1, \tag{7}$$

$$c_1 = c_L \tag{8}$$

The reflected S-wave is labelled $n = 2$, and we have

$$d_1^{(2)} = \cos\theta_2, \quad d_2^{(2)} = \sin\theta_2 \tag{9}$$

$$p_1^{(2)} = \sin\theta_2, \quad p_2^{(2)} = -\cos\theta_2, \tag{10}$$

$$c_1 = c_T \tag{11}$$

By using the traction free boundary condition, we have

$$\tau_{22} = \tau_{21} = 0, \quad x_2 = 0 \tag{12}$$

The parameters of the reflected P-wave and S-wave can be determined

$$k_1 = k_0, \tag{13}$$

$$k_2/k_0 = c_L/c_T = \kappa, \tag{14}$$

$$\theta_1 = \theta_0, \tag{15}$$

$$\sin\theta_2 = \kappa^{-1}\sin\theta_0 \tag{16}$$

$$\frac{A_1}{A_0} = \frac{\sin 2\theta_0 \sin 2\theta_2 - \kappa^2 \cos^2 2\theta_2}{\sin 2\theta_0 \sin 2\theta_2 + \kappa^2 \cos^2 2\theta_2} \tag{17}$$

$$\frac{A_2}{A_0} = \frac{2\kappa \sin 2\theta_0 \cos 2\theta_2}{\sin 2\theta_0 \sin 2\theta_2 + \kappa^2 \cos^2 2\theta_2} \tag{18}$$

Therefore, once the incident waveform is given, the total displacement along the interface can be obtained as

$$\vec{U} = \vec{U}^{(0)} + \vec{U}^{(1)} + \vec{U}^{(2)} \tag{19}$$